PERGAMON

International Journal of Solids and Structures 40 (2003) 1337–1367

INTERNATIONAL JOURNAL OF SOLIDS and STRUCTURES

www.elsevier.com/locate/ijsolstr

The effect of annealing on the viscoplastic response of semicrystalline polymers at finite strains

A.D. Drozdov *, J. deC. Christiansen

Department of Production, Aalborg University, Fibigerstraede 16, Aalborg DK-9220, Denmark

Received 17 July 2002; received in revised form 27 October 2002

Abstract

A constitutive model is developed for the viscoplastic behavior of a semicrystalline polymer at finite strains. A solid polymer is treated as an equivalent heterogeneous network of chains bridged by permanent junctions (physical cross-links, entanglements and lamellar blocks). The network is thought of as an ensemble of meso-regions linked with each other. In the sub-yield region of deformations, junctions between chains in meso-domains slide with respect to their reference positions (which reflects sliding of nodes in the amorphous phase and fine slip of lamellar blocks). Above the yield point, this sliding process is accompanied by displacements of meso-domains in the ensemble with respect to each other (which reflects coarse slip and disintegration of lamellar blocks). To account for the orientation of lamellar blocks in the direction of maximal stresses and formation of micro-fibrils in the post-yield region of deformations (which is observed as strain-hardening of specimens) elastic moduli are assumed to depend on the principal invariants of the right Cauchy–Green tensor for the viscoplastic flow. Stress–strain relations for a semicrystalline polymer are derived by using the laws of thermodynamics. The constitutive equations are determined by six adjustable parameters that are found by matching observations in uniaxial tensile tests on injection-molded isotactic polypropylene at elongations up to 80%. Prior to testing, the specimens were annealed at various temperatures ranging from 110 to 163 °C. Fair agreement is demonstrated between the experimental data and the results of numerical simulation. The effect of annealing temperature on the material parameters is studied in detail.

Keywords: Semicrystalline polymers; Isotactic polypropylene; Finite viscoplasticity; Annealing

1. Introduction

This paper is concerned with modelling the viscoplastic behavior of semicrystalline polymers at isothermal deformations with finite strains. This subject has been a focus of attention in the past decade, which may be explained by the importance of yielding and the post-yield viscoplastic flow in solid polymers for the analysis of fibre-drawing and film-drawing processes (Alberola et al., 1995a,b; Ajji et al., 1996; Buckley

* Corresponding author. Present address: Department of Chemical Engineering, West Virginia University, P.O. Box 6102, Morgantown, WV 26506, USA. Fax: +1-304-293-4139.

E-mail address: Aleksey.Drozdov@mail.wvu.edu (A.D. Drozdov).

0020-7683/02/$ - see front matter © 2002 Elsevier Science Ltd. All rights reserved.
PII: S0020-7683(02)00660-1

et al., 1996; Sweeney and Ward, 1996; Matthews et al., 1997; Sweeney et al., 1997; Sabbagh and Lesser, 1999; Sweeney et al., 1999; Suzuki et al., 1999; Ran et al., 2001).

In the experimental analysis, we concentrate on the mechanical response of injection-molded isotactic polypropylene (iPP). This choice may be explained by numerous applications of polypropylene in industry (ranging from oriented films for packaging to non-woven fabrics and reinforcing fibres).

IPP is a semicrystalline polymer containing three basic crystallographic forms (Iijima and Strobl, 2000): monoclinic α crystallites, (pseudo) hexagonal β structures, orthorhombic γ polymorphs, and "smectic" mesophase (arrays of chains with a better order in the longitudinal than in transverse chain direction). At rapid cooling of the melt (which is typical of the injection-molding process), α crystallites and smectic mesophase are mainly developed, whereas β and γ polymorphs are observed as minority components (Kalay and Bevis, 1997).

The characteristic size of α spherulites in an injection-molded specimen is estimated as 100–200 μm (Kalay and Bevis, 1997; Coulon et al., 1998). These structures are formed by lamellae stacks with lamellar thicknesses ranging from 10 to 20 nm (Coulon et al., 1998; Maiti et al., 2000). A unique feature of the crystalline morphology of iPP is the lamellar cross-hatching: development of transverse lamellae oriented in the direction perpendicular to the direction of radial lamellae in spherulites (Iijima and Strobl, 2000).

Transmission electron microscopy (Yamada et al., 1998; Maiti et al., 2000) and polarized optical microscopy (Yamada et al., 1998) show that annealing of iPP at elevated temperatures results in

1. a decrease in the concentration of transverse lamellae (and total disappearance of cross-hatching at annealing above 150 °C),
2. an increase in the fraction of ordered α crystallites (where helices in monoclinic unit cells are oriented in the same direction).

Recent wide-angle X-ray scattering (WAXS) measurements (Maiti et al., 2000; Gu et al., 2002) reveal that annealing of iPP in the vicinity of the critical temperature $T_c \approx 157$–159 °C induces a second-order phase transition in which the ordered α form is replaced by a new form with a larger lattice volume and higher molecular mobility. As mobility of chains plays the key role in the non-linear mechanical response of solid polymers, this phase transformation strongly affects the viscoplastic behavior of iPP. Our observations show that thermal treatment of iPP at temperatures above T_c noticeably improves its drawability at ambient temperature. Under uniaxial tension, necking of an injection-molded sample occurs at the longitudinal Hencky strain $\epsilon_H = 0.2$. After annealing of a specimen at temperatures about 110–130 °C, the Hencky strain for necking grows up to 0.35, whereas a specimen annealed at 160 °C does not reveal necking at elongations up to $\epsilon_H = 0.6$ (Drozdov and Christiansen, 2002a).

Transformations in the crystalline structure of iPP driven by plastic deformations were recently studied by Aboulfaraj et al. (1995), Coulon et al. (1998), Seguela et al. (1999), Staniek et al. (1999), Zhang et al. (1999), Nitta and Takayanagi (1999, 2000), Ran et al. (2001), Lima et al. (2002) and Seguela (2002), to mention a few. It is found that stretching of a semicrystalline polymer below the yield point induces interlamellar separation, rotation and twist of lamellae, fine slip of lamellar blocks (homogeneous shear of layer-like crystalline structures) (Aboulfaraj et al., 1995; Gaucher-Miri and Seguela, 1997; Hiss et al., 1999; Seguela et al., 1999), chain slip through the crystals, sliding and breakage of tie chains (Nitta and Takayanagi, 1999), and activation of the rigid amorphous fraction (part of the amorphous phase located in regions surrounded by radial and transverse lamellae) (Verma et al., 1996). Deformation in the post-yield region causes coarse slip (heterogeneous inter-lamellar sliding) of lamellar blocks and their fragmentation, detachment of chain folds and loops from the interfaces of crystal blocks, and formation of a fibrillar texture (Gaucher-Miri and Seguela, 1997). Finally, at large strains, breakage of spherulites results in cavitation (Zhang et al., 1999), large-scale separation of lamellar blocks and transformation of spherulites

into the fibrillar form (Nitta and Takayanagi, 2000), and stress-induced crystallization of chains in the amorphous phase (Zhang et al., 1999).

It is hard to believe that these morphological transformations in a semicrystalline polymer can be adequately described by a constitutive model with a relatively small number of adjustable parameters. To develop stress–strain relations, a method of homogenization is applied, according to which a sophisticated micro-structure is replaced by a single phase "whose internal micromechanical state is tracked as a function of applied deformation" (Bergström et al., 2002). As the equivalent phase, the amorphous phase (a network of macromolecules) is conventionally chosen (Sweeney and Ward, 1996; Sweeney et al., 1997, 1999; Boyce et al., 2000; Bergström et al., 2002) for the following reasons:

1. The time-dependent response of solid polymers is associated with rearrangement of chains in amorphous regions.
2. The viscoplastic flow in semicrystalline polymers is "initiated in the amorphous phase before transitioning into the crystalline phase" (Meyer and Pruitt, 2001).
3. Sliding of tie chains along and their detachment from lamellae play the key role in the yielding phenomenon (Nitta and Takayanagi, 1999).

Conventional network theories for the mechanical behavior of semicrystalline polymers at finite strains are grounded on three main assumptions:

1. To develop stress–strain relations in an explicit form, a network is treated as incompressible. Observations show that polypropylene is a compressible polymer, but its degree of compressibility is relatively low (the growth of the tensile strain up to 8% results in an increase in the volume strain by less than 1% (Meddad and Fisa, 1997). In what follows, iPP is modelled as an incompressible medium.
2. To simplify the derivation of constitutive equations, a network is thought of as homogeneous. This assumption contradicts observations in standard relaxation and creep tests that demonstrate a wide spectrum of relaxation (retardation) times. The latter means that the network is composed of a number of meso-domains, where stresses relax with various rates (Sweeney et al., 1999). In this study, an equivalent network is treated as strongly heterogeneous, and it is thought of as en ensemble of meso-regions (MRs) that can slip with respect to each other in the post-yield region of deformations.
3. To apply conventional methods of the hyperelasticity theory, a polymeric network is considered as isotropic. This assumption can be adopted at moderate strains, when sliding of tie chains along lamellar surfaces and fine slip of lamellar blocks do not affect molecular orientation. At higher strains, when orientation of lamellar blocks and chain folds along maximal stresses results in texture formation, this hypothesis becomes inappropriate. In order to take into account the orientation process, we assume that elastic moduli of MRs are substantially affected by plastic strains.

A semicrystalline polymer is thought of as a network of macromolecules bridged by junctions (entanglements, physical cross-links and lamellar blocks). All nodes are treated as permanent (chains cannot separate from junctions during the experimental time-scale), which implies that the viscoelastic phenomena associated with rearrangement of chains are excluded from the consideration. To describe the viscoplastic effects, the network is assumed to deform non-affinely: junctions can slide with respect to their reference positions under loading.

Conventional models in viscoplasticity presume that the response is merely elastic at relatively small strains, whereas the plastic flow begins when the stress intensity exceeds the yield stress. This hypothesis is not applicable to semicrystalline polymers that demonstrate a strongly anelastic behavior at deformations far below the yield point [observed as a pronounce discrepancy between the loading and retraction paths of stress–strain curves in cyclic tests with maximal strains that are substantially lower than the yield strain

(Drozdov and Christiansen, 2003)]. This means that the viscoplastic flow takes place in the sub-yield, as well as in the post-yield regions of deformation. To distinguish between the mechanical responses in these two regions (and to define the yield point in terms of the sliding mechanism), we postulate that sliding of nodes with respect to their reference positions occurs without dissipation of mechanical energy in the sub-yield region, and it leads to a substantial dissipation of energy at straining above the yield point. A detailed discussion of this issue is presented in Section 6.

The objective of the present study is two-fold:

1. To report experimental data in uniaxial tensile tests with finite strains on iPP specimens annealed at several temperatures ranging from 110 to 163 °C.
2. To develop constitutive equations for the viscoplastic behavior of a semicrystalline polymer and to determine adjustable parameters in the stress–strain relations by fitting the observations.

This work concentrates on the viscoplastic behavior of isotactic polypropylene observed in tensile tests with a constant rate of strain. The influence of the strain rate on material parameters is analyzed in another study (Drozdov and Christiansen, 2002b). Constitutive equations for the viscoplastic response of semicrystalline polymers in cyclic tests with small strains have been recently developed in Drozdov and Christiansen (2003).

The exposition is organized as follows. Experimental data in uniaxial tensile tests are reported in Section 2. Kinematic relations for sliding of junctions at finite strains are developed in Section 3. Kinetic equations for the rate-of-strain tensor (that describes sliding of junctions in amorphous regions and fine slip of lamellar blocks in crystalline domains) are formulated in Section 4. Strain energy density of a semicrystalline polymer is determined in Section 5. Constitutive equations for an isothermal deformation with finite strains and kinetic relations for coarse slip and fragmentation of lamellar blocks are derived in Section 6. Phenomenological expressions for material functions are proposed in Section 7. The governing equations are simplified for uniaxial tension of an incompressible medium in Section 8. Adjustable parameters in the stress–strain relations are determined in Section 9 by matching the experimental data. A brief discussion of our findings is presented in Section 10. Some concluding remarks are formulated in Section 11.

2. Experimental procedure

IPP (Novolen 1100L) was supplied by BASF (Targor). ASTM dumbbell specimens were injection molded with length 148 mm, width 9.8 mm and thickness 3.8 mm. Uniaxial tensile tests were performed at room temperature on a testing machine Instron-5568 equipped with electro-mechanical sensors for the control of longitudinal strains in the active zone of samples. The tensile force was measured by a standard load cell. The engineering stress, σ, was determined as the ratio of the axial force to the cross-sectional area of stress-free specimens. The true longitudinal stress, Σ, was calculated with the help of the incompressibility condition as

$$\Sigma = \sigma k,$$

where k is the elongation ratio.

The series of experiments consisted of 10 tests on a sample that was not subjected to thermal treatment and on specimens annealed for 24 h at the temperatures $T = 110$, 120, 130, 140, 145, 150, 155, 158 and 163 °C and slowly cooled by air. To minimize the effect of physical aging, mechanical tests were carried out one day after thermal treatment.

Specimens were stretched with the cross-head speed 30 mm/min (which corresponds to the Hencky strain rate $\dot{\epsilon}_{\rm H} = 6.24 \times 10^{-3}$ s^{-1}) up to the maximal Hencky strain, $\epsilon_{\rm H\,max} = 0.6$. The chosen cross-head speed

ensures nearly isothermal experimental conditions (Inberg et al., 2002), on the one hand, and it allows the viscoelastic effects to be neglected, on the other (the duration of a test does not exceed 70 s).

Every test was performed on a new specimen. The samples that were not subjected to thermal treatment and were annealed in the low-temperatures interval (below the critical temperature $T_{cr} = 155$ °C) demonstrated pronounced necking. No necking of samples was observed in tensile tests on the specimens annealed above T_{cr}.

The true longitudinal stress, Σ, is plotted versus the elongation ratio, k, in Figs. 1–10. These figures show that the stress, Σ, strongly increases with k in the sub-yield region (where the stress–strain curves noticeably

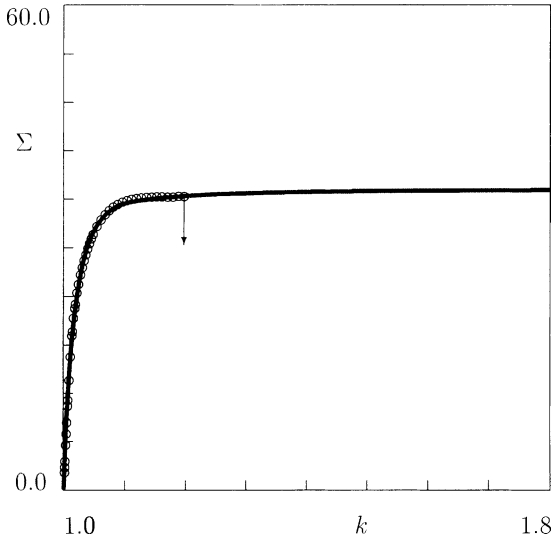

Fig. 1. The true longitudinal stress Σ MPa versus the elongation ratio k. Circles: experimental data on a non-annealed specimen. Vector indicates the beginning of necking. Solid line: results of numerical simulation.

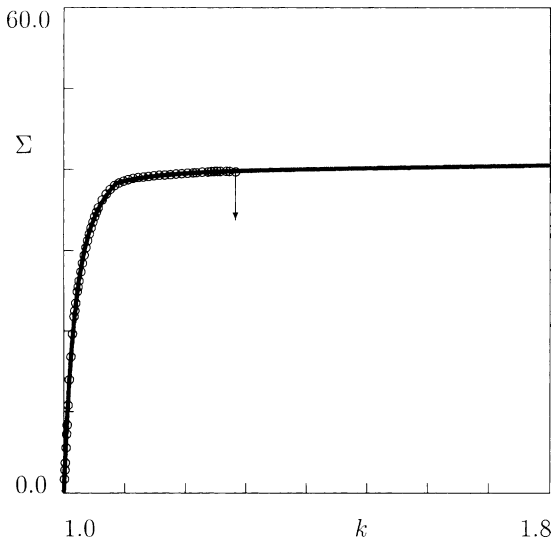

Fig. 2. The true longitudinal stress Σ MPa versus the elongation ratio k. Circles: experimental data on a specimen annealed for 24 h at $T = 110$ °C. Vector indicates the beginning of necking. Solid line: results of numerical simulation.

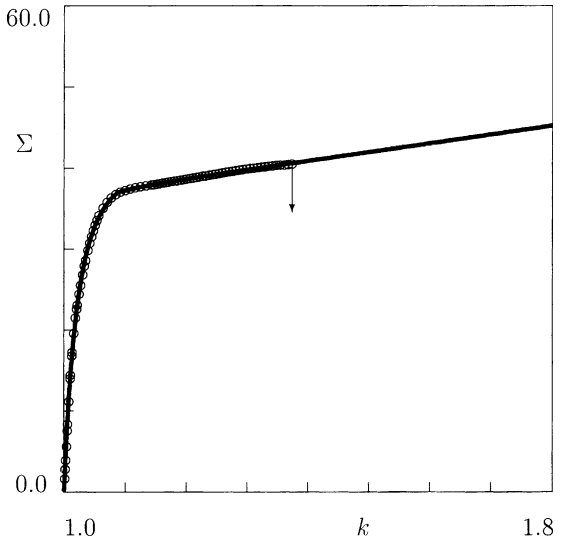

Fig. 3. The true longitudinal stress Σ MPa versus the elongation ratio k. Circles: experimental data on a specimen annealed for 24 h at $T = 120$ °C. Vector indicates the beginning of necking. Solid line: results of numerical simulation.

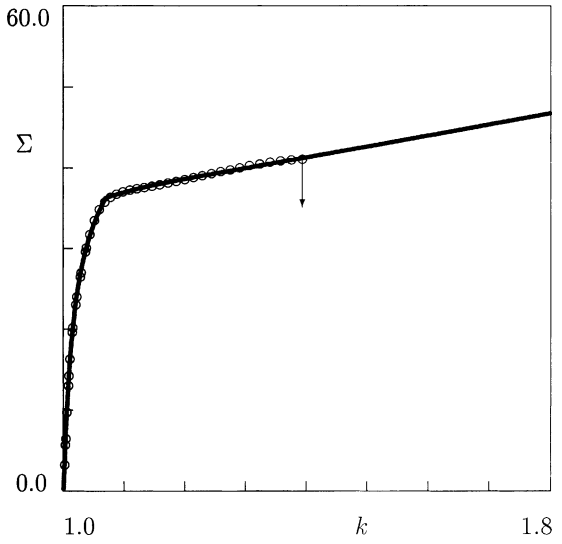

Fig. 4. The true longitudinal stress Σ MPa versus the elongation ratio k. Circles: experimental data on a specimen annealed for 24 h at $T = 130$ °C. Vector indicates the beginning of necking. Solid line: results of numerical simulation.

differ from the straight lines corresponding to the response of an elastic medium) and grows (practically linearly) with the elongation ratio, k, in the post-yield region of deformations.

The elongation ratio for yielding, k_y, is plotted versus the annealing temperature, T, in Fig. 11. This figure shows that k_y monotonically decreases with T. The experimental data are correctly approximated by the phenomenological equation

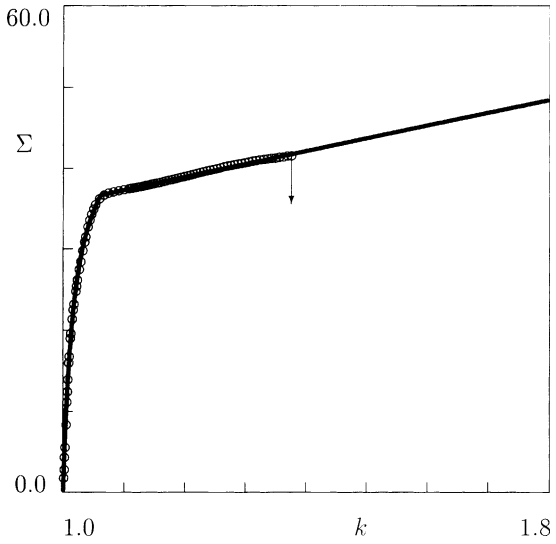

Fig. 5. The true longitudinal stress Σ MPa versus the elongation ratio k. Circles: experimental data on a specimen annealed for 24 h at $T = 140$ °C. Vector indicates the beginning of necking. Solid line: results of numerical simulation.

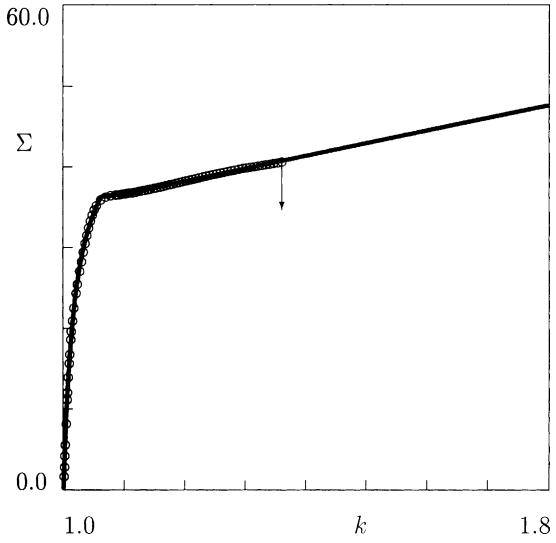

Fig. 6. The true longitudinal stress Σ MPa versus the elongation ratio k. Circles: experimental data on a specimen annealed for 24 h at $T = 145$ °C. Vector indicates the beginning of necking. Solid line: results of numerical simulation.

$$k_y = h_0 - h_1 T, \tag{1}$$

where the coefficients h_m $(m = 0, 1)$ are found by the least-squares algorithm.

The true yield stress, Σ_y, and the true stress for necking, Σ_n, are depicted in Fig. 12. This figure demonstrates that the yield stress monotonically decreases with annealing temperature below T_{cr} and increases

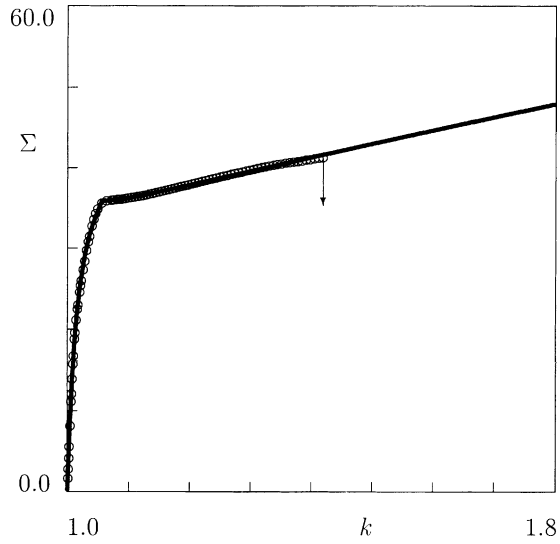

Fig. 7. The true longitudinal stress Σ MPa versus the elongation ratio k. Circles: experimental data on a specimen annealed for 24 h at $T = 150$ °C. Vector indicates the beginning of necking. Solid line: results of numerical simulation.

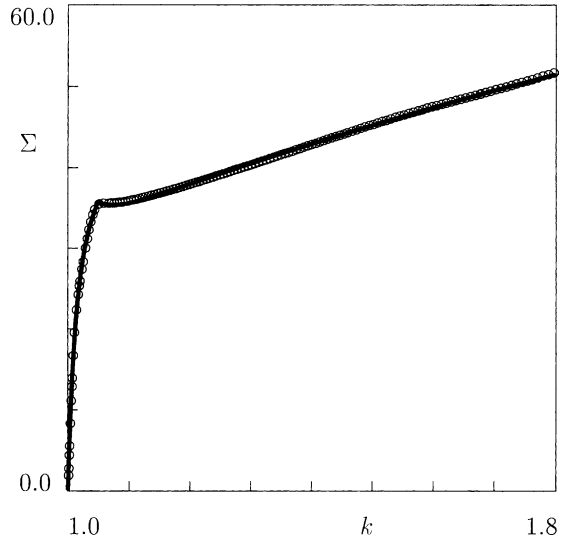

Fig. 8. The true longitudinal stress Σ MPa versus the elongation ratio k. Circles: experimental data on a specimen annealed for 24 h at $T = 155$ °C. Solid line: results of numerical simulation.

in the post-critical region of annealing temperatures. The stress for necking increases with T at temperatures lower than T_{cr}, whereas samples annealed at temperatures above T_{cr} do not reveal necking at the longitudinal strains under consideration. The experimental data are fitted by the phenomenological relations

$$\Sigma_y = S_{y0} + S_{y1}T, \quad \Sigma_n = S_{n0} + S_{n1}T, \tag{2}$$

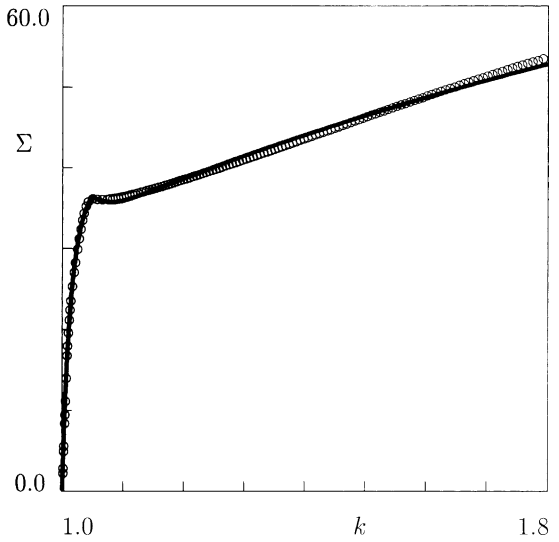

Fig. 9. The true longitudinal stress Σ MPa versus the elongation ratio k. Circles: experimental data on a specimen annealed for 24 h at $T = 158$ °C. Solid line: results of numerical simulation.

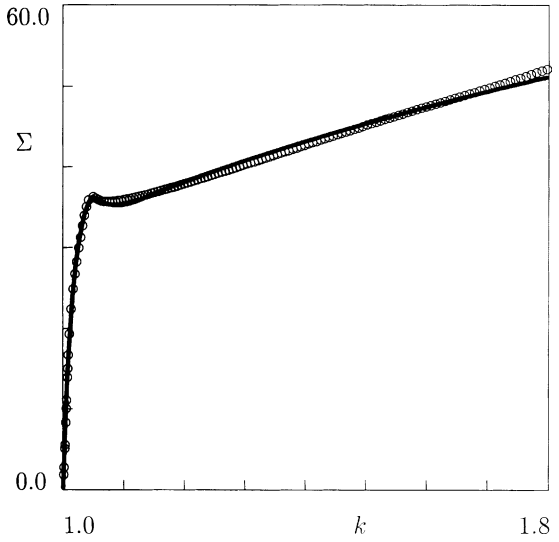

Fig. 10. The true longitudinal stress Σ MPa versus the elongation ratio k. Circles: experimental data on a specimen annealed for 24 h at $T = 163$ °C. Solid line: results of numerical simulation.

where the adjustable parameters S_{ym} and S_{nm} $(m = 0, 1)$ are determined by the least-squares technique. Fig. 12 demonstrates fair agreement between the observations and their approximations by Eq. (2) with different values of S_{ym} below and above the critical temperature T_{cr}.

Our aim now is to derive constitutive equations for the viscoplastic behavior of a semicrystalline polymer that correctly approximate the experimental data depicted in Figs. 1–10.

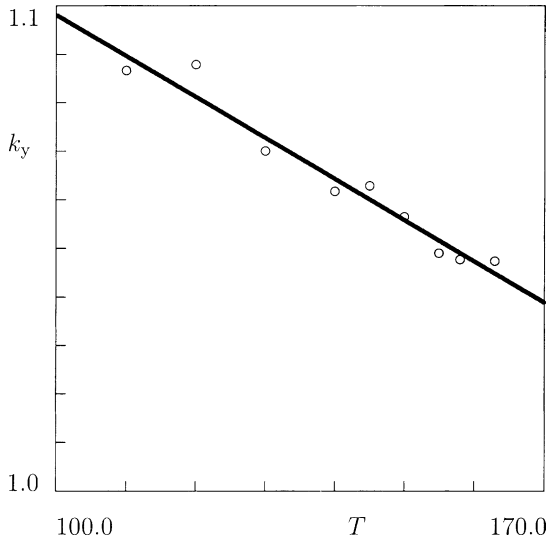

Fig. 11. The elongation ratio for yielding k_y versus the annealing temperature T °C. Circles: treatment of observations. Solid line: approximation of the experimental data by Eq. (1) with $h_0 = 1.18$ and $h_1 = 8.47 \times 10^{-4}$.

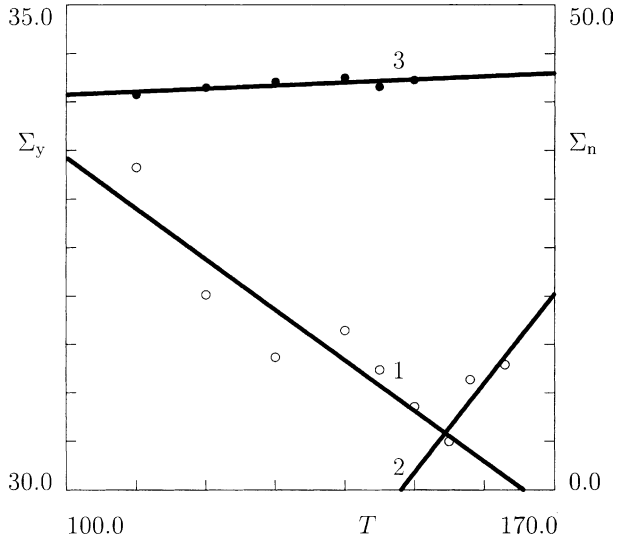

Fig. 12. The true yield stress Σ_y MPa (unfilled circles) and the true stress for necking Σ_n MPa (filled circles) versus the annealing temperature T °C. Symbols: observations. Solid lines: approximation of the experimental data by Eq. (2). Curve 1: $S_{y0} = 43.65$, $S_{y1} = -5.22 \times 10^{-2}$; curve 2: $S_{y0} = 21.35$, $S_{y1} = 9.22 \times 10^{-2}$; curve 3: $S_{n0} = 37.56$, $S_{n1} = 3.19 \times 10^{-2}$.

3. Kinematics of sliding

Denote by $\mathbf{r}_0$ the radius vector of an arbitrary point in the reference state and by $\mathbf{r}(t)$ its radius vector in the deformed state at time $t \geqslant 0$. Transition from the reference state of a network to its actual state is determined by the deformation gradient

$$\mathbf{F}(t) = \frac{\partial \mathbf{r}(t)}{\partial \mathbf{r}_0}. \tag{3}$$

Sliding of junctions in the network with respect to their reference positions is modelled as a transformation of the reference state, when a point with the initial radius vector $\mathbf{r}_0$ moves to the point with a radius vector $\mathbf{r}_s(t)$. This transformation is described by the deformation gradient

$$\mathbf{F}_s(t) = \frac{\partial \mathbf{r}_s(t)}{\partial \mathbf{r}_0}.$$

With reference to the conventional concepts in non-linear mechanics (Haupt, 2000), we suppose that a smooth mapping $\mathbf{r}_s(t, \mathbf{r}_0)$ is determined only locally, which does not require the new (intermediate) configuration to be Euclidean.

A semicrystalline polymer is modelled as an incompressible medium, which implies that its deformation from the reference state to the deformed state is isochoric (volume-preserving). We suppose that transformation of the initial reference state into the new reference state (that is characterized by the deformation gradient $\mathbf{F}_s$) is volume-preserving as well.

Transformation of the new reference state into the deformed state is determined by the deformation gradient

$$\mathbf{F}_e(t) = \frac{\partial \mathbf{r}(t)}{\partial \mathbf{r}_s(t)}.$$

The subscript indices "s" and "e" indicate that appropriate deformation gradients describe sliding of junctions and elastic deformation (the latter means that the strain energy density is a function of $\mathbf{F}_e$).

According to the chain rule for differentiation, the tensors $\mathbf{F}(t)$, $\mathbf{F}_s(t)$ and $\mathbf{F}_e(t)$ are connected by the relationship

$$\mathbf{F}(t) = \mathbf{F}_e(t) \cdot \mathbf{F}_s(t), \tag{4}$$

where the dot denotes inner product. Formula (4) coincides with the multiplicative presentation of the deformation gradient proposed by Buckley et al. (1996), where $\mathbf{F}_e$ is called the "network stretch" tensor and $\mathbf{F}_s$ is identified as the "slippage stretch" tensor.

Differentiation of Eq. (3) with respect to time implies that

$$\frac{d\mathbf{F}}{dt}(t) = \frac{\partial \mathbf{v}(t)}{\partial \mathbf{r}_0} = \frac{\partial \mathbf{v}(t)}{\partial \mathbf{r}(t)} \cdot \frac{\partial \mathbf{r}(t)}{\partial \mathbf{r}_0},$$

where $\mathbf{v}(t) = d\mathbf{r}(t)/dt$ is the velocity vector. Introducing the velocity gradient

$$\mathbf{L}(t) = \frac{\partial \mathbf{v}(t)}{\partial \mathbf{r}(t)},$$

and using Eq. (3), we obtain

$$\frac{d\mathbf{F}}{dt}(t) = \mathbf{L}(t) \cdot \mathbf{F}(t). \tag{5}$$

Bearing in mind that

$$\frac{d\mathbf{F}^{-1}}{dt}(t) = -\mathbf{F}^{-1}(t) \cdot \frac{d\mathbf{F}}{dt}(t) \cdot \mathbf{F}^{-1}(t),$$

we find from Eq. (5) that

$$\frac{d\mathbf{F}^{-1}}{dt}(t) = -\mathbf{F}^{-1}(t)\cdot\mathbf{L}(t). \tag{6}$$

By analogy with Eqs. (5) and (6), we write

$$\frac{d\mathbf{F}_s}{dt}(t) = \mathbf{L}_s(t)\cdot\mathbf{F}_s(t), \quad \frac{d\mathbf{F}_s^{-1}}{dt}(t) = -\mathbf{F}_s^{-1}(t)\cdot\mathbf{L}_s(t), \tag{7}$$

where

$$\mathbf{L}_s(t) = \frac{\partial\mathbf{v}_s(t)}{\partial\mathbf{r}_s(t)}$$

is the velocity gradient for sliding of junctions, and $\mathbf{v}_s(t) = d\mathbf{r}_s(t)/dt$.

It follows from Eq. (4) that

$$\frac{d\mathbf{F}_e}{dt}(t) = \frac{d}{dt}\left[\mathbf{F}(t)\cdot\mathbf{F}_s^{-1}(t)\right] = \frac{d\mathbf{F}}{dt}(t)\cdot\mathbf{F}_s^{-1}(t) + \mathbf{F}(t)\cdot\frac{d\mathbf{F}_s^{-1}}{dt}(t).$$

Substitution of Eqs. (5) and (7) into this equality results in

$$\frac{d\mathbf{F}_e}{dt}(t) = \mathbf{L}(t)\cdot\mathbf{F}_e(t) - \mathbf{F}_e(t)\cdot\mathbf{L}_s(t). \tag{8}$$

The left and right Cauchy–Green tensors for elastic deformation are given by

$$\mathbf{B}_e(t) = \mathbf{F}_e(t)\cdot\mathbf{F}_e^T(t), \quad \mathbf{C}_e(t) = \mathbf{F}_e^T(t)\cdot\mathbf{F}_e(t), \tag{9}$$

where T stands for transpose. We differentiate the second equality in Eq. (9) with respect to time, use Eq. (8), and find that

$$\frac{d\mathbf{C}_e}{dt}(t) = 2\mathbf{F}_e^T(t)\cdot\mathbf{D}(t)\cdot\mathbf{F}_e(t) - \mathbf{L}_s^T(t)\cdot\mathbf{C}_e(t) - \mathbf{C}_e(t)\cdot\mathbf{L}_s(t), \tag{10}$$

where

$$\mathbf{D}(t) = \frac{1}{2}\left[\mathbf{L}(t) + \mathbf{L}^T(t)\right] \tag{11}$$

is the rate-of-strain tensor. Taking into account that

$$\frac{d\mathbf{C}_e^{-1}}{dt}(t) = -\mathbf{C}_e^{-1}(t)\cdot\frac{d\mathbf{C}_e}{dt}(t)\cdot\mathbf{C}_e^{-1}(t),$$

and using Eq. (10), we arrive at the formula

$$\frac{d\mathbf{C}_e^{-1}}{dt}(t) = -2\mathbf{F}_e^{-1}(t)\cdot\mathbf{D}(t)\cdot[\mathbf{F}_e^{-1}(t)]^T + \mathbf{C}_e^{-1}(t)\cdot\mathbf{L}_s^T(t) + \mathbf{L}_s(t)\cdot\mathbf{C}_e^{-1}(t). \tag{12}$$

The first principal invariant of the right Cauchy–Green tensor $\mathbf{C}_e(t)$ reads

$$J_1(t) = \mathscr{I}_1(\mathbf{C}_e(t)) = \mathbf{C}_e(t) : \mathbf{I},$$

where $\mathscr{I}_1$ stands for the first invariant of a tensor, $\mathbf{I}$ is the unit tensor and the colon stands for convolution. Differentiating this equality with respect to time and employing Eqs. (9) and (10), we obtain

$$\frac{dJ_1}{dt}(t) = 2[\mathbf{B}_e(t) : \mathbf{D}(t) - \mathbf{C}_e(t) : \mathbf{D}_s(t)], \tag{13}$$

where

$$\mathbf{D}_{\mathrm{s}}(t)=\frac{1}{2}\left[\mathbf{L}_{\mathrm{s}}(t)+\mathbf{L}_{\mathrm{s}}^{\mathrm{T}}(t)\right] \tag{14}$$

is the rate-of-strain tensor for sliding of junctions. For an incompressible medium, the second principal invariant of the right Cauchy–Green tensor $\mathbf{C}_{\mathrm{e}}(t)$ is given by

$$J_2(t)=\mathscr{I}_1(\mathbf{C}_{\mathrm{e}}^{-1}(t))=\mathbf{C}_{\mathrm{e}}^{-1}(t):\mathbf{I}.$$

Differentiation of this equality with respect to time and use of Eqs. (9) and (12) imply that

$$\frac{\mathrm{d}J_2}{\mathrm{d}t}(t)=-2\left[\mathbf{B}_{\mathrm{e}}^{-1}(t):\mathbf{D}(t)-\mathbf{C}_{\mathrm{e}}^{-1}(t):\mathbf{D}_{\mathrm{s}}(t)\right]. \tag{15}$$

It follows from Eqs. (12) and (15) that the derivative of an arbitrary smooth function, $\Phi(J_1,J_2)$, of the first two principal invariants of the right Cauchy–Green tensor, $\mathbf{C}_{\mathrm{e}}(t)$, is determined by the formula

$$\frac{\mathrm{d}\Phi}{\mathrm{d}t}(J_1(t),J_2(t))=2\left\{\left[\Phi_1(t)\mathbf{B}_{\mathrm{e}}(t)-\Phi_2(t)\mathbf{B}_{\mathrm{e}}^{-1}(t)\right]:\mathbf{D}(t)-\left[\Phi_1(t)\mathbf{C}_{\mathrm{e}}(t)-\Phi_2(t)\mathbf{C}_{\mathrm{e}}^{-1}(t)\right]:\mathbf{D}_{\mathrm{s}}(t)\right\}, \tag{16}$$

where

$$\Phi_m(t)=\frac{\partial\Phi}{\partial J_m}(J_1(t),J_2(t))\quad(m=1,2). \tag{17}$$

To describe strain-hardening of a semicrystalline polymer under active loading in the post-yield region of deformations, we introduce the deformation gradient, $\mathbf{f}(t)$, from the reference state at the yielding point to the reference state at time $t\geqslant t_{\mathrm{y}}$, where t_{y} is the instant when yielding occurs. The tensor $\mathbf{f}(t)$ reads

$$\mathbf{f}(t)=\mathbf{F}_{\mathrm{s}}(t)\cdot\mathbf{F}_{\mathrm{s}}^{-1}(t_{\mathrm{y}}). \tag{18}$$

It follows from Eqs. (7) and (18) that this tensor obeys the linear differential equation

$$\frac{\mathrm{d}\mathbf{f}}{\mathrm{d}t}(t)=\mathbf{L}_{\mathrm{s}}(t)\cdot\mathbf{f}(t),\quad\mathbf{f}(t_{\mathrm{y}})=\mathbf{I}. \tag{19}$$

By analogy with Eq. (9), we introduce the left and right Cauchy–Green tensors for the post-yield transformation of the reference state

$$\mathbf{b}(t)=\mathbf{f}(t)\cdot\mathbf{f}^{\mathrm{T}}(t),\quad\mathbf{c}(t)=\mathbf{f}^{\mathrm{T}}(t)\cdot\mathbf{f}(t). \tag{20}$$

Differentiating the second equality in Eq. (20) and using Eqs. (18) and (19), we obtain

$$\frac{\mathrm{d}\mathbf{c}}{\mathrm{d}t}(t)=2\mathbf{f}^{\mathrm{T}}(t)\cdot\mathbf{D}_{\mathrm{s}}(t)\cdot\mathbf{f}(t). \tag{21}$$

Taking into account that

$$\frac{\mathrm{d}\mathbf{c}^{-1}}{\mathrm{d}t}(t)=-\mathbf{c}^{-1}(t)\cdot\frac{\mathrm{d}\mathbf{c}}{\mathrm{d}t}(t)\cdot\mathbf{c}^{-1}(t),$$

we find from Eq. (21) that

$$\frac{\mathrm{d}\mathbf{c}^{-1}}{\mathrm{d}t}(t)=-2\mathbf{f}^{-1}(t)\cdot\mathbf{D}_{\mathrm{s}}(t)\cdot[\mathbf{f}^{-1}(t)]^{\mathrm{T}}. \tag{22}$$

As any transformation of the reference state is volume preserving, the first two principal invariants of the tensor $\mathbf{c}(t)$ are given by

$$j_1(t)=\mathbf{c}(t):\mathbf{I},\quad j_2(t)=\mathbf{c}^{-1}(t):\mathbf{I}. \tag{23}$$

Differentiating the first equation in Eq. (23) with respect to time and using Eqs. (20) and (21), we arrive at the formula

$$\frac{\mathrm{d}j_1}{\mathrm{d}t}(t) = 2\mathbf{b}(t) : \mathbf{D}_{\mathrm{s}}(t). \tag{24}$$

Similarly, Eqs. (20), (22) and (23) imply that

$$\frac{\mathrm{d}j_2}{\mathrm{d}t}(t) = -2\mathbf{b}^{-1}(t) : \mathbf{D}_{\mathrm{s}}(t). \tag{25}$$

It follows from Eqs. (24) and (25) that the derivative of an arbitrary smooth function, $\phi(j_1, j_2)$, of the principal invariants of the right Cauchy–Green tensor, $\mathbf{c}(t)$, reads

$$\frac{\mathrm{d}\phi}{\mathrm{d}t}(j_1(t), j_2(t)) = 2\big[\phi_1(t)\mathbf{b}(t) - \phi_2(t)\mathbf{b}^{-1}(t)\big] : \mathbf{D}_{\mathrm{s}}(t), \tag{26}$$

where

$$\phi_m(t) = \frac{\partial\phi}{\partial j_m}(j_1(t), j_2(t)) \quad (m = 1, 2). \tag{27}$$

It is worth noting that Eqs. (20), (23) and (26) are valid for any $t \geqslant t_{\mathrm{y}}$. In the sub-yield region of deformations, when $t < t_{\mathrm{y}}$, we set formally

$$\frac{\mathrm{d}\phi}{\mathrm{d}t}(j_1(t), j_2(t)) = 0, \quad \mathbf{b}(t) = \mathbf{c}(t) = \mathbf{I}, \quad j_1(t) = j_2(t) = 3. \tag{28}$$

Our aim now is to establish connections between the rate-of-strain tensor for sliding of junctions, $\mathbf{D}_{\mathrm{s}}(t)$, on the one hand, and the rate-of-strain tensor for macro-deformation, $\mathbf{D}(t)$, and some tensors that characterize elastic deformation of a polymer, on the other.

4. Kinetics of fine slip

A semicrystalline polymer is treated as a strongly heterogeneous network of chains. The network is modelled as an ensemble of MRs with arbitrary shapes. The characteristic length of a MR substantially exceeds the radius of gyration for a macromolecule, and it is noticeably less than a size of a sample.

Deformation of a specimen induces two sliding processes in the network:

1. Sliding of junctions (physical cross-links and entanglements between chains in a network) with respect to their reference positions in stress-free meso-domains.
2. Sliding of MRs in the ensemble with respect to each other.

Sliding of nodes in meso-domains of an equivalent network reflects (i) sliding of junctions between chains in the amorphous phase, (ii) slippage of tie chains along lamellar surfaces (Nitta and Takayanagi, 1999), and (iii) fine slip of lamellar blocks (homogeneous shearing of layer-like crystallites and their relative displacements) (Hiss et al., 1999).

Sliding of MRs with respect to each other reflects (i) coarse slip of lamellae (inter-lamellar sliding), (ii) fragmentation of lamellae into mosaic blocks linked by tie chains, and (iii) their alignment along the direction of maximal stresses (Hiss et al., 1999).

To describe changes in the microstructure of semicrystalline polymers driven by simultaneous effects of these two processes, we introduce two rate-of-strain tensors, $\mathbf{D}_{\mathrm{f}}$ and $\mathbf{D}_{\mathrm{c}}$, and adopt the conventional assumption that the total rate-of-strain tensor, $\mathbf{D}_{\mathrm{s}}$, equals the sum of $\mathbf{D}_{\mathrm{f}}$ and $\mathbf{D}_{\mathrm{c}}$,

$$\mathbf{D}_s = \mathbf{D}_f + \mathbf{D}_c, \tag{29}$$

where the subscript indices "f" and "c" refer to fine and coarse slip, respectively.

Stretching of a specimen induces sliding of junctions in amorphous domains and fine slip of lamellar blocks in crystalline domains both in the sub-yield and post-yield regions of deformation. As a first guess, it is natural to assume the rate-of-strain tensor, $\mathbf{D}_f$, to be proportional to the rate-of-strain tensor, $\mathbf{D}$, for macro-deformation,

$$\mathbf{D}_f(t) = \alpha(t)\mathbf{D}(t), \tag{30}$$

where the coefficient of proportionality, α, is a function of the principal invariants, J_1 and J_2, of the right Cauchy–Green tensor $\mathbf{C}_e$ (the third principal invariant of $\mathbf{C}_e$ is excluded from the consideration due to the incompressibility condition).

We suppose that the coefficient α vanishes at the zero elastic strain, monotonically increases with elastic deformation, and tends to some constant $a \in [0,1]$ (the rate of sliding of junctions for a developed plastic flow) for relatively large elastic strains. The inequality $a \geqslant 0$ means that junctions slide in the direction determined by the macro-strain, whereas the condition $a \leqslant 1$ ensures that the rate of sliding of nodes does not exceed the rate of macro-strain.

The following advantages of relationship (30) are worth to be mentioning:

1. Eq. (30) is linear (which means that the rate of sliding of junctions is proportional to the rate of macro-strain),
2. this formula involves the only adjustable function, $\alpha(t)$,
3. it implies that flow of junctions satisfies the incompressibility condition, $\mathscr{I}_1(\mathbf{D}_f) = 0$, provided that the polymer is incompressible, $\mathscr{I}_1(\mathbf{D}) = 0$.

A substantial shortcoming of Eq. (30) is that it does not satisfy the objectivity condition (Haupt, 2000). Indeed, superposition of a rigid rotation in the actual state, $\mathbf{r}(t) \to \mathbf{r}^\circ(t) = \mathbf{O}(t) \cdot \mathbf{r}(t)$, where $\mathbf{O}(t)$ is an orthogonal tensor, implies that the rate-of-strain tensor for macro-deformation, $\mathbf{D}(t)$, is replaced by the tensor

$$\mathbf{D}^\circ(t) = \mathbf{O}(t) \cdot \mathbf{D}(t) \cdot \mathbf{O}^T(t), \tag{31}$$

whereas the rate-of-strain tensor, $\mathbf{D}_f(t)$, remains unchanged.

In order to develop an analog of Eq. (30) that is consistent with the axioms of continuum mechanics, on the one hand, and that preserves (at least, partially) the advantages of Eq. (30), we employ the right polar decomposition of the deformation gradient for transition from the current reference state into the deformed state,

$$\mathbf{F}_e(t) = \mathbf{R}_e(t) \cdot \mathbf{U}_e(t), \tag{32}$$

where $\mathbf{R}_e(t)$ is an orthogonal rotation tensor,

$$\mathbf{R}_e^T(t) = \mathbf{R}_e^{-1}(t), \tag{33}$$

and $\mathbf{U}_e(t)$ is a symmetric stretch tensor that satisfies the equality

$$\mathbf{U}_e^2(t) = \mathbf{C}_e(t). \tag{34}$$

Bearing in mind that under rigid rotation in the deformed state, $\mathbf{r}(t) \to \mathbf{r}^\circ(t)$, the tensor $\mathbf{R}_e(t)$ is transformed into the tensor

$$\mathbf{R}_e^\circ(t) = \mathbf{O}(t) \cdot \mathbf{R}_e(t), \tag{35}$$

we replace Eq. (30) by the kinetic equation

$$\mathbf{D}_{\mathrm{f}}(t) = \alpha(t)\mathbf{R}_{\mathrm{e}}^{\mathrm{T}}(t) \cdot \mathbf{D}(t) \cdot \mathbf{R}_{\mathrm{e}}(t). \tag{36}$$

The advantages of Eq. (36) are that

1. this formula is transformed into linear kinetic equation (30) at small strains (when the tensor $\mathbf{R}_{\mathrm{e}}(t)$ may be replaced by the unit tensor $\mathbf{I}$),
2. relationship (36) obeys the objectivity condition (this assertion follows from Eqs. (31) and (35)).

Eqs. (33) and (36) imply that for isochoric (volume-preserving) macro-deformations (when the first principal invariant of the tensor $\mathbf{D}$ vanishes), the first principal invariant of the tensor $\mathbf{D}_{\mathrm{f}}$ equals zero as well. Indeed,

$$\mathscr{I}_1(\mathbf{D}_{\mathrm{f}}) = \alpha\mathscr{I}_1(\mathbf{R}_{\mathrm{e}}^{\mathrm{T}} \cdot \mathbf{D} \cdot \mathbf{R}_{\mathrm{e}}) = \alpha\mathscr{I}_1(\mathbf{R}_{\mathrm{e}} \cdot \mathbf{R}_{\mathrm{e}}^{\mathrm{T}} \cdot \mathbf{D}) = \alpha\mathscr{I}_1(\mathbf{D}) = 0. \tag{37}$$

It follows from Eqs. (9), (32), (34), (36) that

$$\begin{aligned}\mathbf{C}_{\mathrm{e}} : \mathbf{D}_{\mathrm{f}} &= \mathscr{I}_1(\mathbf{C}_{\mathrm{e}} \cdot \mathbf{D}_{\mathrm{f}}) = \alpha\mathscr{I}_1(\mathbf{U}_{\mathrm{e}}^2 \cdot \mathbf{R}_{\mathrm{e}}^{\mathrm{T}} \cdot \mathbf{D} \cdot \mathbf{R}_{\mathrm{e}}) = \alpha\mathscr{I}_1(\mathbf{R}_{\mathrm{e}} \cdot \mathbf{U}_{\mathrm{e}} \cdot (\mathbf{R}_{\mathrm{e}} \cdot \mathbf{U}_{\mathrm{e}})^{\mathrm{T}} \cdot \mathbf{D}) = \alpha\mathscr{I}_1(\mathbf{F}_{\mathrm{e}} \cdot \mathbf{F}_{\mathrm{e}}^{\mathrm{T}} \cdot \mathbf{D}) \\ &= \alpha\mathscr{I}_1(\mathbf{B}_{\mathrm{e}} \cdot \mathbf{D}) = \alpha\mathbf{B}_{\mathrm{e}} : \mathbf{D}.\end{aligned} \tag{38}$$

By analogy with Eq. (38), we find that

$$\mathbf{C}_{\mathrm{e}}^{-1} : \mathbf{D}_{\mathrm{f}} = \alpha\mathbf{B}_{\mathrm{e}}^{-1} : \mathbf{D}. \tag{39}$$

Combining Eqs. (16), (29) and (36) and using Eqs. (38) and (39), we arrive at the formula for the derivative of an arbitrary smooth function, $\Phi(J_1, J_2)$, with respect to time,

$$\frac{\mathrm{d}\Phi}{\mathrm{d}t}(J_1(t), J_2(t)) = 2\big\{[1 - \alpha(t)]\big[\Phi_1(t)\mathbf{B}_{\mathrm{e}}(t) - \Phi_2(t)\mathbf{B}_{\mathrm{e}}^{-1}(t)\big] : \mathbf{D}(t) - \big[\Phi_1(t)\mathbf{C}_{\mathrm{e}}(t) - \Phi_2(t)\mathbf{C}_{\mathrm{e}}^{-1}(t)\big] : \mathbf{D}_{\mathrm{c}}(t)\big\}, \tag{40}$$

where the functions Φ_m $(m = 1, 2)$ are determined by Eq. (17).

Substitution of Eqs. (29) and (36) into Eq. (26) implies that in the post-yield region of deformations, when $t \geqslant t_{\mathrm{y}}$, for an arbitrary smooth function, $\phi(j_1, j_2)$,

$$\begin{aligned}\frac{\mathrm{d}\phi}{\mathrm{d}t}(j_1(t), j_2(t)) = 2\big\{&\alpha(t)\big[\mathbf{R}_{\mathrm{e}}(t) \cdot \big(\phi_1(t)\mathbf{b}(t) - \phi_2(t)\mathbf{b}^{-1}(t)\big) \cdot \mathbf{R}_{\mathrm{e}}^{\mathrm{T}}(t)\big] : \mathbf{D}(t) \\ &+ (\phi_1(t)\mathbf{b}(t) - \phi_2(t)\mathbf{b}^{-1}(t)) : \mathbf{D}_{\mathrm{c}}(t)\big\},\end{aligned} \tag{41}$$

where the functions ϕ_m $(m = 1, 2)$ are given by Eq. (27).

Our purpose now is to determine the mechanical energy of a semicrystalline polymer and to calculate its derivative with respect to time using Eqs. (40) and (41).

5. Strain energy density

An equivalent network of chains is thought of as an ensemble of MRs connected with each other by links (crystalline lamellae) that transmit the macro-strain to individual meso-domains.

A MR in the ensemble is treated as an incompressible isotropic medium with the strain energy density (per unit volume)

$$\tilde{w} = \mu w,$$

where μ is an average rigidity of a meso-domain and $w = w(J_1, J_2)$ is a smooth dimensionless function that satisfies the condition

$$w(J_1, J_2)|_{J_1=3, J_2=3} = 0.$$

This equality means that the mechanical energy of a MR vanishes in the reference state.

The rigidity, μ, is assumed to be constant below the yield point, and to increase with viscoplastic strains in the post-yield region. In the latter case, μ becomes a function of the principal invariants of the right Cauchy–Green tensor $\mathbf{c}$: $\mu = \mu(j_1, j_2)$. The dependence of μ on j_m $(m = 1, 2)$ reflects strain-hardening of a semicrystalline polymer driven by texture formation above the yield point.

Neglecting the energy of interaction between MRs, we calculate the strain energy density per unit volume of a semicrystalline polymer, W, as the sum of the mechanical energies of MRs,

$$W(t) = M(j_1(t), j_2(t)) w(J_1(t), J_2(t)), \tag{42}$$

where $M = \mu N$, and N is the average number of meso-domains per unit volume. The function $M(j_1, j_2)$ stands for the rigidity of a network per unit volume.

Differentiating Eq. (42) with respect to time, using Eqs. (28) and (40), and bearing in mind that the first principal invariant of the rate-of-strain tensor, $\mathbf{D}$, vanishes for isochoric deformations, we find that in the sub-yield region of deformations, when $t < t_y$,

$$\frac{dW}{dt}(t) = 2\mathbf{A}'(t) : \mathbf{D}(t), \tag{43}$$

where

$$\mathbf{A}(t) = M(3,3)[1 - \alpha(t)]\left[w_1(t)\mathbf{B}_e(t) - w_2(t)\mathbf{B}_e^{-1}(t)\right], \tag{44}$$

the prime stands for the deviatoric component of a tensor, and

$$w_m(t) = \frac{\partial w}{\partial J_m}(J_1(t), J_2(t)) \quad (m = 1, 2). \tag{45}$$

Eqs. (41) and (42) together with the condition that the first principal invariants of the rate-of-strain tensors, $\mathbf{D}$ and $\mathbf{D}_c$, equal zero for volume-preserving transformations imply that in the post-yield region of deformations, when $t \geqslant t_y$,

$$\frac{dW}{dt}(t) = 2\left[\mathbf{A}'(t) : \mathbf{D}(t) - \mathbf{A}_c'(t) : \mathbf{D}_c(t)\right], \tag{46}$$

where

$$\begin{aligned}
&\mathbf{A}(t) = M_0(t)[1 - \alpha(t)]\left[w_1(t)\mathbf{B}_e(t) - w_2(t)\mathbf{B}_e^{-1}(t)\right] + \alpha(t) w_0(t)\mathbf{R}_e(t) \cdot \left[M_1(t)\mathbf{b}(t) - M_2(t)\mathbf{b}^{-1}(t)\right] \cdot \mathbf{R}_e^{T}, \\
&\mathbf{A}_c(t) = M_0(t)\left[w_1(t)\mathbf{C}_e(t) - w_2(t)\mathbf{C}_e^{-1}(t)\right] - w_0(t)\left[M_1(t)\mathbf{b}(t) - M_2(t)\mathbf{b}^{-1}(t)\right].
\end{aligned} \tag{47}$$

The functions $w_0(t)$ and $M_m(t)$ read

$$w_0(t) = w(J_1(t), J_2(t)), \quad M_0(t) = M(j_1(t), j_2(t)), \quad M_m(t) = \frac{\partial M}{\partial j_m}(j_1(t), j_2(t)) \quad (m = 1, 2). \tag{48}$$

Eqs. (43) and (46) will be applied to derive stress–strain relations and kinetic equations for the evolution of the rate-of-strain tensor, $\mathbf{D}_c(t)$, by using the laws of thermodynamics.

6. Constitutive equations

For isothermal deformation of an incompressible medium, the Clausius–Duhem inequality reads (Haupt, 2000)

$$Q(t) = -\frac{dW}{dt}(t) + \mathbf{\Sigma}'(t) : \mathbf{D}(t) \geqslant 0, \tag{49}$$

where $\mathbf{\Sigma}$ is the Cauchy stress tensor, and Q is the internal dissipation per unit volume.

Substitution of Eq. (43) into Eq. (49) implies that in the sub-yield region of deformations, when $t < t_y$,

$$Q(t) = [\mathbf{\Sigma}(t) - 2\mathbf{A}(t)]' : \mathbf{D}(t) \geqslant 0. \tag{50}$$

It follows from Eq. (44) that below the yield point, the Clausius–Duhem inequality (50) is satisfied, provided that the Cauchy stress tensor is given by

$$\mathbf{\Sigma}(t) = -p(t)\mathbf{I} + 2M(3,3)[1-\alpha(t)]\big[w_1(t)\mathbf{B}_e(t) - w_2(t)\mathbf{B}_e^{-1}(t)\big], \tag{51}$$

where $p(t)$ is pressure. In this case, the internal dissipation in the network, Q, vanishes.

Combining Eqs. (46) and (49), we find the internal dissipation in the post-yield region, when $t \geqslant t_y$,

$$Q(t) = [\mathbf{\Sigma}(t) - 2\mathbf{A}(t)]' : \mathbf{D}(t) + 2\mathbf{A}_c'(t) : \mathbf{D}_c(t) \geqslant 0. \tag{52}$$

Equating the expression in the square brackets to zero and using Eq. (47), we arrive at the stress–strain relation for the response of a semicrystalline polymer in the post-yield region,

$$\begin{aligned}\mathbf{\Sigma}(t) = -p(t)\mathbf{I} + 2\big\{&M_0(t)[1-\alpha(t)][w_1(t)\mathbf{B}_e(t) - w_2(t)\mathbf{B}_e^{-1}(t)] \\ &+ \alpha(t)w_0(t)\mathbf{R}_e(t)\cdot[M_1(t)\mathbf{b}(t) - M_2(t)\mathbf{b}^{-1}(t)]\cdot\mathbf{R}_e^{T}(t)\big\}.\end{aligned} \tag{53}$$

Eqs. (52) and (53) imply that the internal dissipation in the post-yield region, when $t \geqslant t_y$, reads

$$Q(t) = \mathbf{A}_c'(t) : \mathbf{D}_c(t) \geqslant 0.$$

It follows from this equality and Eq. (47) that the Clausius–Duhem inequality is satisfied, provided that

$$\mathbf{D}_c(t) = 2\gamma(t)\big\{M_0(t)[w_1(t)\mathbf{C}_e(t) - w_2(t)\mathbf{C}_e^{-1}(t)] - w_0(t)\big[M_1(t)\mathbf{b}(t) - M_2(t)\mathbf{b}^{-1}(t)\big]\big\}', \tag{54}$$

where $\gamma(t)$ is a non-negative scalar function.

The viscoplastic response of a semicrystalline polymer is determined by the stress–strain relations (51) and (53) together with the kinetic Eqs. (29), (36) and (54) for sliding of junctions in amorphous regions and fine and coarse slip of lamellar blocks in the crystalline domains. To complete the set of constitutive equations, we should establish a correspondence between the vorticity tensor for sliding of junctions $\mathbf{\Omega}_s(t) = \frac{1}{2}[\mathbf{L}_s - \mathbf{L}_s^{T}(t)]$ and the vorticity tensor for macro-deformation $\mathbf{\Omega}(t) = \frac{1}{2}[\mathbf{L} - \mathbf{L}^{T}(t)]$. We do not dwell, however, on such a relationship, because the present study concentrates on uniaxial tension of an incompressible medium, when both tensors, $\mathbf{\Omega}$ and $\mathbf{\Omega}_s$, vanish.

The governing equations (29), (36), (51), (53), (54) are determined by four adjustable functions: $\alpha(t)$, $M(j_1, j_2)$, $w(J_1, J_2)$ and $\gamma(t)$. Our aim now is to propose phenomenological relations for these functions and to discuss their applicability to matching the experimental data depicted in Figs. 1–10.

7. Material functions

We begin with the dimensionless strain energy density, w, and set

$$w = J_1 - 3. \tag{55}$$

Eq. (55) describes the mechanical energy of a neo-Hookean medium. The advantages of this equation are that (i) it contains no adjustable parameters, and (ii) Eq. (55) has a transparent physical meaning as the strain energy density of a Gaussian network of flexible chains.

The following phenomenological relation is proposed for the function $\alpha(t)$:

$$\alpha = a\left[1 - \exp\left(-\frac{\sqrt{J_1 - 3}}{\varepsilon}\right)\right]. \tag{56}$$

Eq. (56) is determined by two adjustable parameters, a and ε, where a is the rate of sliding of junctions for a developed plastic flow and ε is a strain that characterizes transition to the steady plastic flow.

The term $J_1 - 3$ in Eq. (56), coincides with the strain energy density of a network of flexible chains (55). As is well known, for uniaxial deformation with small strains, the mechanical energy of a neo–Hookean medium is reduced to the square of the elastic strain, ϵ_e^2. This implies that for uniaxial tension with small strains, Eq. (56) reads

$$\alpha = a\left[1 - \exp\left(-\frac{\epsilon_e}{\varepsilon_*}\right)\right], \tag{57}$$

where, in general, the strain ε_* does not necessary coincides with ε. Equation (57) was successfully employed in our previous study on the viscoplastic response of iPP at small strains (Drozdov and Christiansen, 2003). Phenomenological relationships similar to Eq. (56) were previously suggested by Kaye and Kennett (1974) and Wagner et al. (1979) to describe the time-dependent response of polyethylene melts at elongational and shear flows.

As we have no a priori information about changes in the elastic modulus, M, induced by texture formation in the post-yield region of deformations, we adopt a conventional approach in non-linear solid mechanics and expand the function $M(j_1, j_2)$ into a Taylor series in the first two principal invariants of the right Cauchy–Green tensor $\mathbf{c}$,

$$M(j_1, j_2) = \frac{1}{2}C\left[1 + \sum_{m,n=1}^{\infty} \eta_{mn}(j_1 - 3)^m (j_2 - 3)^n\right],$$

where C is an analog of the conventional rigidity per unit volume and η_{mn} are non-negative dimensionless coefficients. To reduce the number of adjustable parameters, it is natural to neglect all terms in the series beyond the first order of smallness, which results in the formula similar to the expression for the strain energy density of a Mooney–Rivlin material

$$M(j_1, j_2) = \frac{1}{2}C[1 + \eta_{10}(j_1 - 3) + \eta_{01}(j_2 - 3)].$$

Our preliminary analysis of the experimental data reveals that the influence of the last term in this equality is negligible. Disregarding this term, we arrive at the formula for the evolution of the elastic modulus driven by strain-hardening,

$$M(j_1, j_2) = \frac{1}{2}C[1 + \eta(j_1 - 3)]. \tag{58}$$

An advantage of Eq. (58) is that it is determined by only two material constants, C and $\eta = \eta_{10}$, to be found by matching observations.

We adopt the standard formulas for the intensity of macro-strain rate, D_i, and the true stress intensity, Σ_i,

$$D_i = \sqrt{\frac{2}{3}\mathbf{D} : \mathbf{D}}, \quad \Sigma_i = \sqrt{\frac{3}{2}\mathbf{\Sigma}' : \mathbf{\Sigma}'}. \tag{59}$$

As this study focuses on experimental data in uniaxial tests, an explicit expression for the yield surface cannot be verified. We accept the von Mises criterion and assume that in the sub-yield region of deformations, when MRs do not slide with respect to each other,

$$\Sigma_i < \Sigma_y, \tag{60}$$

whereas in the post-yield region, when coarse slip and fragmentation of lamellar blocks occurs,

$$\Sigma_i \geqslant \Sigma_y. \tag{61}$$

To describe the effect of mechanical factors on the coefficient γ in Eq. (54), we suppose that γ is proportional to the intensity of macro-strain rate, D_i, which means that coarse slip and fragmentation of lamellar blocks occur under active deformation only,

$$\gamma(t) = \gamma_0(t) D_i(t).$$

With reference to the theory of thermo-mechanically activated processes (Eyring, 1936), the viscoplastic flow in the post-yield region is assumed to be accelerated by stresses. Adopting the Eyring formula for the rate of lamellar disintegration driven by mechanical factors, we set

$$\gamma_0(t) = \gamma_* \exp\left[b(\Sigma_i(t) - \Sigma_y)\right],$$

where γ_* is an attempt rate and b is a positive coefficient. Combining these relationships, we arrive at the formula

$$\gamma(t) = \gamma_* \exp\left[b(\Sigma_i(t) - \Sigma_y)\right] D_i(t). \tag{62}$$

Substitution of expressions (55), (58) and (62) into the constitutive Eqs. (29), (36), (51), (53), (54) implies that in the sub-yield region of deformations, see Eq. (60),

$$\begin{aligned} &\mathbf{\Sigma}(t) = -p(t)\mathbf{I} + C[1 - \alpha(t)]\mathbf{B}_e(t), \\ &\mathbf{D}_s(t) = \alpha(t)\mathbf{R}_e^T(t) \cdot \mathbf{D}(t) \cdot \mathbf{R}_e(t), \end{aligned} \tag{63}$$

and in the post-yield region of deformations, see Eq. (61),

$$\begin{aligned} &\mathbf{\Sigma}(t) = -p(t)\mathbf{I} + C\{[1 - \alpha(t)][1 + \eta(j_1(t) - 3)]\mathbf{B}_e(t) + \eta\alpha(t)(J_1(t) - 3)\mathbf{R}_e(t) \cdot \mathbf{b}(t) \cdot \mathbf{R}_e^T(t)\}, \\ &\mathbf{D}_s(t) = \alpha(t)\mathbf{R}_e^T(t) \cdot \mathbf{D}(t) \cdot \mathbf{R}_e(t) + \gamma_* C D_i(t) \exp\left[b(\Sigma_i(t) - \Sigma_y)\right]\{[1 + \eta(j_1(t) - 3)]\mathbf{C}_e(t) - \eta(J_1(t) - 3)\mathbf{b}(t)\}'. \end{aligned} \tag{64}$$

Eqs. (56), (63) and (64) provide stress–strain relations for a semicrystalline polymer at an arbitrary deformation with finite strains. These equations involve six adjustable parameters: a, b, C, γ_*, η and ε. This number of material constants is quite comparable with those used in other constitutive relations in viscoplasticity of solid polymers (Boyce et al., 1988; Bordonaro and Krempl, 1995; Hasan and Boyce, 1995; Buckley et al., 1996; Matthews et al., 1997; Spathis and Kontou, 1998).

Our aim now is to simplify the stress–strain relations for uniaxial tension of an incompressible medium.

8. Uniaxial tension

Points of a bar refer to Cartesian coordinates $\{X_i\}$ $(i = 1, 2, 3)$ in the stress-free state, to Cartesian coordinates $\{x_i\}$ in the deformed state, and to Cartesian coordinates $\{\xi_i\}$ in the reference state at time t. Uniaxial tension of the incompressible medium is described by the formulas

$$x_1 = k(t)X_1, \quad x_2 = k^{-\frac{1}{2}}(t)X_2, \quad x_3 = k^{-\frac{1}{2}}(t)X_3, \tag{65}$$

where $k = k(t)$ is an elongation ratio. It is assumed that transformation of the reference state is determined by the equations similar to Eq. (65),

$$\xi_1 = \kappa(t)X_1, \quad \xi_2 = \kappa^{-\frac{1}{2}}(t)X_2, \quad \xi_3 = \kappa^{-\frac{1}{2}}(t)X_3, \tag{66}$$

where $\kappa(t)$ is a function to be found. It follows from Eqs. (65) and (66) that

$$\mathbf{B}_e = \mathbf{C}_e = \left(\frac{k}{\kappa}\right)^2 \mathbf{e}_1\mathbf{e}_1 + \frac{\kappa}{k}(\mathbf{e}_2\mathbf{e}_2 + \mathbf{e}_3\mathbf{e}_3), \tag{67}$$

where $\mathbf{e}_i$ are base vectors of the Cartesian frame $\{X_i\}$. Eqs. (32), (34) and (67) imply that

$$\mathbf{R}_e = \mathbf{I}.$$

By analogy with Eq. (67), we find that in the post-yield region of deformations,

$$\mathbf{b} = \mathbf{c} = \left(\frac{\kappa}{\kappa_y}\right)^2 \mathbf{e}_1\mathbf{e}_1 + \frac{\kappa_y}{\kappa}(\mathbf{e}_2\mathbf{e}_2 + \mathbf{e}_3\mathbf{e}_3), \tag{68}$$

where κ_y is the value of κ at the yield point.

Substitution of Eqs. (67) and (68) into Eqs. (63) and (64) results in

$$\mathbf{\Sigma} = \Sigma_1\mathbf{e}_1\mathbf{e}_1 + \Sigma_2(\mathbf{e}_2\mathbf{e}_2 + \mathbf{e}_3\mathbf{e}_3).$$

The non-zero components of the Cauchy stress tensor, Σ_1 and Σ_2, are given by

$$\Sigma_1 = -p(k,\kappa) + C[1 - \alpha(k,\kappa)]\left(\frac{k}{\kappa}\right)^2,$$

$$\Sigma_2 = -p(k,\kappa) + C[1 - \alpha(k,\kappa)]\frac{\kappa}{k}$$

below the yield point, and

$$\Sigma_1 = -p(k,\kappa,\kappa_y) + C\left\{[1 - \alpha(k,\kappa)][1 + \eta(j_1(\kappa,\kappa_y) - 3)]\left(\frac{k}{\kappa}\right)^2 + \eta\alpha(k,\kappa)(J_1(k,\kappa) - 3)\left(\frac{\kappa}{\kappa_y}\right)^2\right\},$$

$$\Sigma_2 = -p(k,\kappa,\kappa_y) + C\left\{[1 - \alpha(k,\kappa)][1 + \eta(j_1(\kappa,\kappa_y) - 3)]\frac{\kappa}{k} + \eta\alpha(k,\kappa)(J_1(k,\kappa) - 3)\frac{\kappa_y}{\kappa}\right\}$$

above the yield point. Excluding the unknown pressure, p, from these equations and the boundary condition on the lateral surface of the bar,

$$\Sigma_2 = 0,$$

we find the only component of the Cauchy stress tensor, the true longitudinal stress $\Sigma = \Sigma_1$. In the sub-yield region of deformations,

$$\Sigma = C[1 - \alpha(k,\kappa)]\left[\left(\frac{k}{\kappa}\right)^2 - \frac{\kappa}{k}\right], \tag{69}$$

and in the post-yield region,

$$\Sigma = C\left\{[1 - \alpha(k,\kappa)][1 + \eta(j_1(\kappa,\kappa_y) - 3)]\left[\left(\frac{k}{\kappa}\right)^2 - \frac{\kappa}{k}\right] + \eta\alpha(k,\kappa)(J_1(k,\kappa) - 3)\left[\left(\frac{\kappa}{\kappa_y}\right)^2 - \frac{\kappa_y}{\kappa}\right]\right\}, \tag{70}$$

where

$$J_1 = \left(\frac{k}{\kappa}\right)^2 + 2\frac{\kappa}{k}, \quad j_1 = \left(\frac{\kappa}{\kappa_y}\right)^2 + 2\frac{\kappa_y}{\kappa}, \tag{71}$$

and the function $\alpha(k,\kappa)$ is given by Eq. (56). Eq. (59) implies that

$$\Sigma_i = \Sigma,$$

which means the Eq. (69) is fulfilled when $\Sigma < \Sigma_y$ and Eq. (70) is satisfied when $\Sigma \geqslant \Sigma_y$.

It follows from Eqs. (11), (14) and (65), (66) that

$$\mathbf{D} = \frac{1}{k}\frac{dk}{dt}\left[\mathbf{e}_1\mathbf{e}_1 - \frac{1}{2}(\mathbf{e}_2\mathbf{e}_2 + \mathbf{e}_3\mathbf{e}_3)\right], \quad \mathbf{D}_s = \frac{1}{\kappa}\frac{d\kappa}{dt}\left[\mathbf{e}_1\mathbf{e}_1 - \frac{1}{2}(\mathbf{e}_2\mathbf{e}_2 + \mathbf{e}_3\mathbf{e}_3)\right]. \tag{72}$$

Eqs. (59) and (72) imply that

$$D_i = \frac{1}{k}\frac{dk}{dt}.$$

Substitution of these expressions into Eqs. (63) and (64) results in the differential equations

$$\frac{d\kappa}{dk} = \alpha(k,\kappa)\frac{\kappa}{k} \quad (\Sigma < \Sigma_y), \tag{73}$$

$$\frac{d\kappa}{dk} = \left\{\alpha(k,\kappa) + \Gamma\exp(b(\Sigma - \Sigma_y))\left[(1 + \eta(j_1(\kappa,\kappa_y) - 3))\left(\left(\frac{k}{\kappa}\right)^2 - \frac{\kappa}{k}\right) - \eta(J_1(k,\kappa) - 3)\right.\right.$$
$$\left.\left.\times\left(\left(\frac{\kappa}{\kappa_y}\right)^2 - \frac{\kappa_y}{\kappa}\right)\right]\right\}\frac{\kappa}{k} \quad (\Sigma \geqslant \Sigma_y), \tag{74}$$

where $\Gamma = \frac{2}{3}\gamma_* C$.

Given a loading program, $k = k(t)$, the longitudinal stress, $\Sigma(t)$, is determined by relations (69) and (70). To calculate the elongation ratio, $\kappa(t)$, that characterizes fine and coarse slips of lamellar blocks, non-linear kinetic Eqs. (73) and (74) are integrated numerically. The constitutive equations involve six parameters to be found by matching experimental data:

1. An analog of the elastic modulus C.
2. The coefficient, η, that characterizes strain-hardening in the post-yield region of deformations.
3. The rate, a, of a developed plastic flow of junctions.
4. The strain, ε, that characterizes transition to the steady plastic flow.
5. The rate, Γ, of coarse slip of lamellar blocks.
6. The coefficient, b, that accounts for the stress-induced acceleration of the viscoplastic flow in the post-yield region.

The yield stress, Σ_y, is determined directly from a stress–strain diagram as the true stress corresponding to the point of maximum on the engineering stress–engineering strain curve. To find the viscoplastic elongation ratio at yielding, κ_y, the governing equations are integrated from $\Sigma = 0$ to $\Sigma = \Sigma_y$.

The following advantages of the constitutive equations should be mentioned:

1. The parameter b that describes mechanically-induced activation of viscoplastic flow in the post-yield region is uniquely determined by the test temperature. This means that this quantity can be found by fitting a stress–strain curve for any specimen and used without changes to approximate experimental data for

other samples. Our preliminary results show that the value $b = 0.04$ MPa^{-1} (that corresponds to an increase in the rate of lamellar fragmentation by a factor of 2 in the range of stresses under consideration) ensures an acceptable quality of matching.
2. Three material constants, C, a and ε, are found by fitting a stress–strain curve below the yield point.
3. After these quantities are determined, the other two parameters, Γ and η, are found in the approximation of the stress–strain curve in the post-yield region of deformations.

Our purpose now is to find the constants a, C, Γ, η and ε by matching the experimental data plotted in Figs. 1–10 and to study the effect of annealing temperature on these quantities.

9. Fitting of observations

We begin with matching the stress–strain diagrams below the yield point. To find the constants C, a and ε, we fix some intervals $[0, a_{\max}]$ and $[0, \varepsilon_{\max}]$, where the "best-fit" parameters a and ε are assumed to be located, and divide these intervals into J subintervals by the points $a^{(i)} = i\Delta a$ and $\varepsilon^{(j)} = j\Delta\varepsilon$ $(i, j = 1, \ldots, J)$ with $\Delta a = a_{\max}/J$ and $\Delta\varepsilon = \varepsilon_{\max}/J$. For any pair, $\{a^{(i)}, \varepsilon^{(j)}\}$, Eqs. (56), (69), (71) and (73) with the initial condition $\kappa(1) = 1$ are integrated numerically by the Runge–Kutta method with the step $\Delta k = 1.0 \times 10^{-5}$ in the interval between $\Sigma = 0$ and $\Sigma = \Sigma_y$. Given a pair, $\{a^{(i)}, \varepsilon^{(j)}\}$, the elastic modulus, C, is found by the least-squares method from the condition of minimum of the function

$$R = \sum_{k_n} \left[\Sigma_{\exp}(k_n) - \Sigma_{num}(k_n)\right]^2,$$

where the sum is calculated over all experimental points, k_n, in the sub-yield interval, $\Sigma_{\exp}$ is the stress measured in a tensile test, and Σ_{num} is given by Eq. (69). The "best-fit" parameters a and ε are determined from the condition of minimum of the function R on the set $\{a^{(i)}, \varepsilon^{(j)}\ (i, j = 1, \ldots, J)\}$.

The material constants C, a and ε that minimize the discrepancies between the experimental data and the results of numerical analysis are found for any stress–strain curve independently. These quantities are plotted versus the annealing temperature, T, in Figs. 13–15. The experimental data are approximated by the linear functions

$$C = C_0 + C_1 T, \quad a = a_0 + a_1 T, \quad \varepsilon = \varepsilon_0 + \varepsilon_1 T, \tag{75}$$

where the coefficients C_m, a_m and ε_m $(m = 0, 1)$ are found by the least-squares technique. Figs. 13–15 demonstrate that the first equation in Eq. (75) provides an acceptable quality of fitting, whereas the other two equations ensure fair agreement between the experimental data and the results of numerical simulation when different constants, a_m and ε_m are used below and above some critical temperature, T_{cr}.

To find the quantities Γ and η, we approximate the stress–strain curves in the post-yield region of deformations. For any set of experimental data, we use the parameters C, a and ε found by fitting an appropriate stress–strain curve in the sub-yield region of deformations. To approximate a stress–strain curve above the yield point, we apply an algorithm similar to that used to match the observations in the sub-yield region of deformations. We fix some intervals $[0, \Gamma_{\max}]$ and $[0, \eta_{\max}]$, where the "best-fit" parameters Γ and η are assumed to be located, and divide these intervals into J subintervals by the points $\Gamma^{(i)} = i\Delta\Gamma$ and $\eta^{(j)} = j\Delta\eta$ $(i, j = 1, \ldots, J)$ with $\Delta\Gamma = \Gamma_{\max}/J$ and $\Delta\eta = \eta_{\max}/J$. Given a pair, $\{\Gamma^{(i)}, \eta^{(j)}\}$, Eqs. (56), (70), (71) and (74) are integrated numerically by the Runge–Kutta method with the step $\Delta k = 1.0 \times 10^{-5}$. The "best-fit" parameters Γ and η are found from the condition of minimum of the function R on the set $\{\Gamma^{(i)}, \eta^{(j)}\ (i, j = 1, \ldots, J)\}$.

Figs. 1–10 demonstrate fair agreement between the experimental data in tensile tests and the results of numerical simulation.

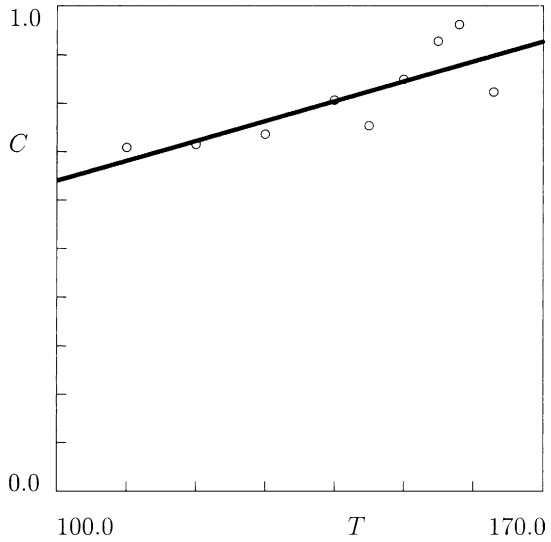

Fig. 13. The elastic modulus C GPa versus the annealing temperature T °C. Circles: treatment of observations. Solid line: approximation of the experimental data by Eq. (75) with $C_0 = 0.23$ and $C_1 = 4.11 \times 10^{-3}$.

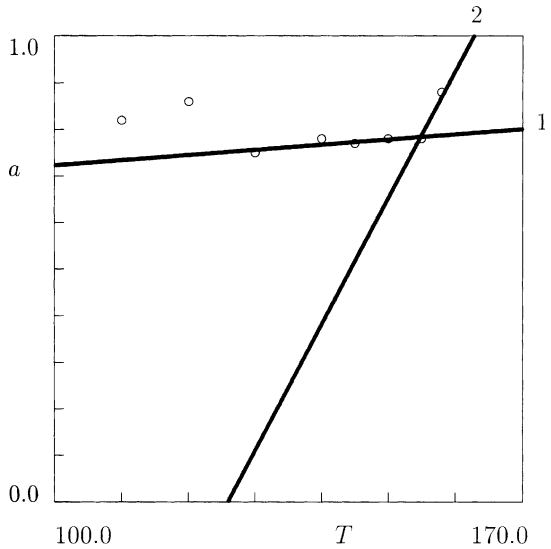

Fig. 14. The rate of developed plastic flow a versus the annealing temperature T °C. Circles: treatment of observations. Solid lines: approximation of the experimental data by Eq. (75). Curve 1: $a_0 = 0.61$, $a_1 = 1.11 \times 10^{-3}$; curve 2: $a_0 = -3.42$, $a_1 = 2.71 \times 10^{-2}$.

The dimensionless parameters, Γ and η, are plotted versus the annealing temperature, T, in Figs. 16 and 17. The experimental data are approximated by the linear functions

$$\Gamma = \Gamma_0 + \Gamma_1 T, \quad \eta = \eta_0 + \eta_1 T, \tag{76}$$

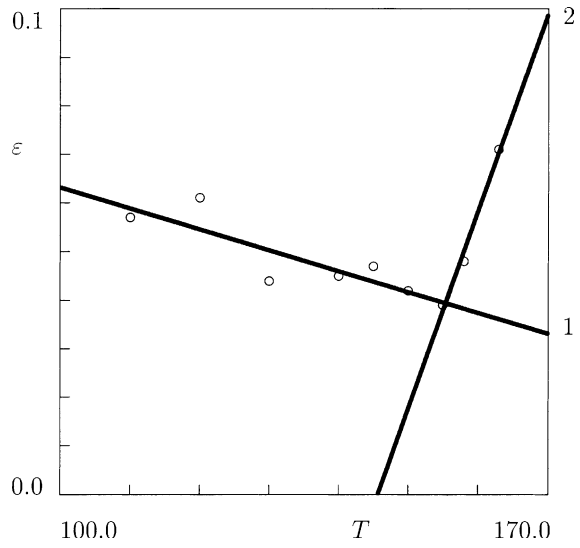

Fig. 15. The strain for transition to a developed plastic flow ε versus the annealing temperature T °C. Circles: treatment of observations. Solid lines: approximation of the experimental data by Eq. (75). Curve 1: $\varepsilon_0 = 0.11$, $\varepsilon_1 = -4.28 \times 10^{-4}$; curve 2: $\varepsilon_0 = -0.59$, $\varepsilon_1 = 4.06 \times 10^{-3}$.

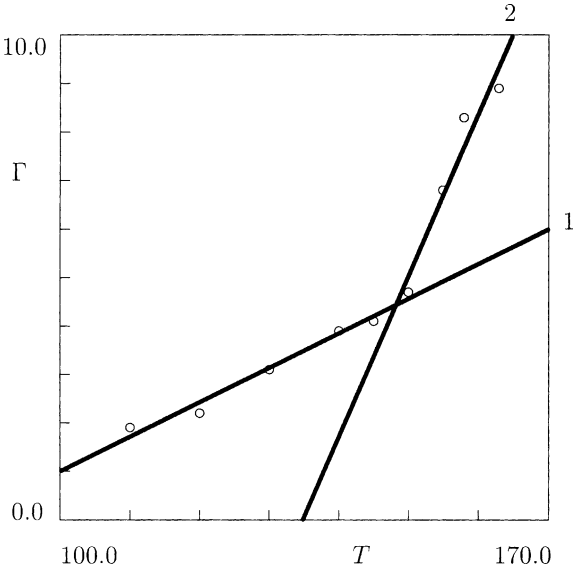

Fig. 16. The dimensionless rate of plastic flow in the post-yield region Γ versus the annealing temperature T °C. Circles: treatment of observations. Solid lines: approximation of the experimental data by Eq. (76). Curve 1: $\Gamma_0 = -6.14$, $\Gamma_1 = 7.14 \times 10^{-2}$; curve 2: $\Gamma_0 = -4.48$, $\Gamma_1 = 3.32 \times 10^{-1}$.

where the coefficients Γ_m and η_m $(m = 0, 1)$ are found by the least-squares algorithm. Figs. 16 and 17 show good quality of matching the observations by Eq. (76) with different coefficients, Γ_m and η_m, below and above the critical temperature, T_{cr}.

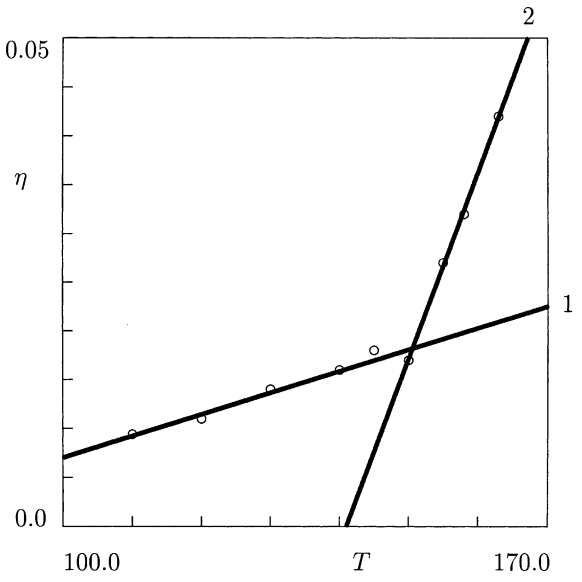

Fig. 17. The coefficient η characterizing strain-hardening versus the annealing temperature T °C. Circles: treatment of observations. Solid lines: approximation of the experimental data by Eq. (76). Curve 1: $\eta_0 = -1.50 \times 10^{-2}$, $\eta_1 = 2.21 \times 10^{-4}$; curve 2: $\eta_0 = -2.69 \times 10^{-1}$, $\eta_1 = 1.91 \times 10^{-3}$.

10. Discussion

According to Fig. 13, the elastic modulus, C, linearly increases with annealing temperature T (the scatter of the data is, however, rather large). This monotonic growth of the elastic modulus may be explained by an increase in the degree of crystallinity of isotactic polypropylene at annealing.

To justify this hypothesis, we performed DSC (differential scanning calorimetry) measurements on a specimen not subjected to thermal treatment and on samples annealed at various temperatures in the range from 110 to 170 °C. Calorimetric tests were carried out on STA 449/Netzsch apparatus with a heating rate of 5 K/min in the range of temperatures from 35 to 200 °C. The specimens with weights of about 15 mg were tested in Al_2O_2 pans covered by lid in argon atmosphere. The thermal analyzer was calibrated with references ranging from In to Ni. The degree of crystallinity, K, was calculated as the ratio of the specific enthalpy of melting of a specimen to the enthalpy of fusion (209 J/g) of a fully crystalline polypropylene (Wunderlich, 1980).

To establish a correspondence between changes in the elastic modulus, C, and the degree of crystallinity, K, we introduce (i) the ratio, r_C, of the elastic modulus of a specimen annealed at a temperature T to that of a non-annealed sample, and (ii) the ratio, r_K, of the degree of crystallinity of a specimen annealed at a temperature T to that of a non-annealed sample. The dimensionless parameters, r_C and r_K, are plotted versus the annealing temperature, T, in Fig. 18. The experimental data are approximated by the phenomenological relations

$$r_C = r_{C0} + r_{C1}T, \quad r_K = r_{K0} + r_{K1}T, \tag{77}$$

where the coefficients r_{Cm} and r_{Km} $(m = 0, 1)$ are found by the least-squares algorithm. The striking similarity of the slopes of curves 1 and 2 in Fig. 18 ($r_{C1} = 5.79 \times 10^{-3}$ and $r_{K1} = 5.24 \times 10^{-3}$) unambiguously proves that changes in the elastic modulus at annealing may be attributed to an increase in the degree of crystallinity of iPP.

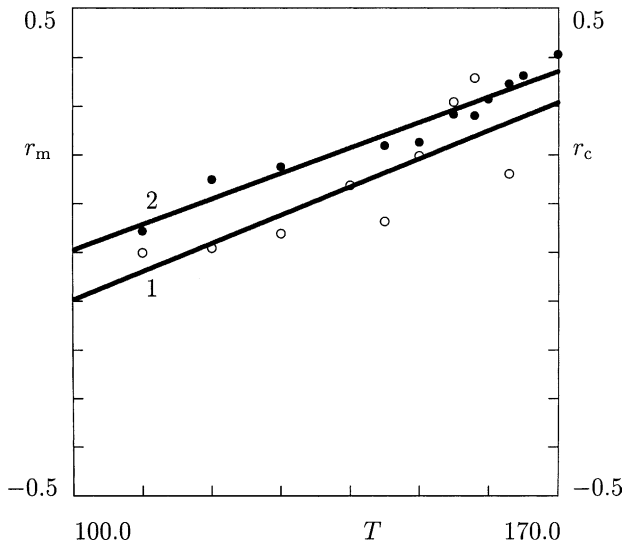

Fig. 18. The dimensionless ratios r_C (unfilled circles) and r_K (filled circles) versus the annealing temperature T °C. Symbols: treatment of observations in mechanical and calorimetric tests. Solid lines: approximation of the experimental data by Eq. (77). Curve 1: $r_{C0} = 0.32$, $r_{C1} = 5.79 \times 10^{-3}$; curve 2: $r_{K0} = 0.48$, $r_{K1} = 5.24 \times 10^{-3}$.

Fig. 14 demonstrates that the rate, a, of the developed plastic flow (associated with sliding of junctions in the amorphous phase and fine slip of lamellar blocks in the crystalline phase) weakly increases with annealing temperature, T, below the critical temperature, T_{cr}, and strongly grows with T in the post-critical region. The weak increase in $a(T)$ in the sub-critical region of temperatures may be explained by a decrease in the content of transverse lamellae with annealing temperature (and their disappearance after thermal treatment at temperatures above 150 °C (Yamada et al., 1998)). This reduction in the fraction of transverse lamellae at annealing enhances deformations in amorphous regions, and, as a consequence, accelerates the viscoplastic flow. The strong growth of the function $a(T)$ in the post-critical region of annealing temperatures may be attributed to the phase transition in the crystalline phase (Maiti et al., 2000; Gu et al., 2002). This transition results in a noticeable expansion of unit cells in crystallites. The latter implies a substantial increase in molecular mobility (Gu et al., 2002), which accelerates fine slip of lamellar blocks.

It is worth noting that the data for specimens annealed at low temperatures, 110 and 120 °C, slightly deviate from curve 1 in Fig. 14. Two possible explanations may be provided for these discrepancies:

1. Thermal treatment of iPP in the range of temperatures between 110 and 130 °C is favorable for nucleation of β crystallites, which are more ductile than α structures, and, as a result, reveal a more pronounced slip of lamellar blocks (Labour et al., 2001).
2. The crystalline phase of iPP contain two populations of lamellar structures: strong (dominant) lamellae and weak (subsidiary) lamellae (Alamo et al., 1999). Secondary crystallization at annealing induces (i) thickening of dominant lamellae and (ii) nucleation and growth of subsidiary lamellae. Both these processes are thermally activated, which means that their rates are noticeably reduced with an increase in the degree of undercooling (the difference between the melting temperature and the temperature of thermal treatment). The latter means that at low temperatures (below 130 °C), 24 h of annealing may be insufficient for formation of subsidiary lamellae that strongly resist sliding of junctions in amorphous regions. As a result, the rates of developed viscoplastic flow in the samples annealed at these temperatures exceed those predicted by curve 1 in Fig. 14.

To check these hypotheses, WAXS measurements were conducted at ambient temperature in forward reflection mode with Philips PW-1830 generator operated at 40 kV and 20 mA with a conventional CuKα X-ray source. The thickness of samples was about 1 mm, the exposure time was 4 h, the diffraction angle 2θ ranged from 10° to 25°. The WAXS diagrams for specimens annealed in the range of temperatures from 110 to 170 °C demonstrate the X-ray diffraction patterns typical of the α polymorph (Iijima and Strobl, 2000; Cho et al., 2002). No peaks in the vicinity of $2\theta = 16.2°$ characteristic for the $\beta(300)$ form (Cho et al., 2002) were observed. The latter indicates that the most probable explanation for high rates of the developed viscoplastic flow in specimens annealed at 110 and 120 °C is a negligible concentration of subsidiary lamellae nucleated during thermal treatment.

Fig. 15 reveals that the strain, ε, that characterizes transition to a developed flow of junctions, decreases with annealing temperature, T, below the critical temperature, T_{cr}. This decrease may be ascribed to a decrease in the number of transverse lamellae at annealing. Disappearance of transverse lamellae results in release in the rigid amorphous fraction (amorphous regions where molecular motion is constrained by surrounding lamellae) and noticeably enhances the sliding process (that occurs at lower elongation ratios). An increase in ε in the post-critical region of temperatures may be attributed to changes in the micromechanism of viscoplastic flow, when sliding of junctions in the amorphous phase is replaced by slip of layer-like structures in the crystalline phase.

According to Fig. 16, the rate of coarse slip and fragmentation of lamellar blocks monotonically increases with annealing temperature. The function $\Gamma(T)$ grows rather slowly below some threshold temperature, $T^0 \approx 150$ °C, and its rate of increase becomes substantially larger above T^0. The threshold temperature, T^0, perfectly coincides with the temperature at which lamellar cross-hatching disappears in iPP (Yamada et al., 1998). Therefore, the alteration of the rate of coarse slip of lamellar blocks at T^0 may be ascribed to melting of transverse lamellae and decay in lamellar branching in α spherulites (Alamo et al., 1999).

A similar explanation may be provided for the increase in the coefficient η reported in Fig. 17. In the low-temperature region of annealing temperatures, only partial melting occurs of transverse lamellae, which implies that in the post-yield region of deformations, most lamellar blocks are not totally separated from surrounding lamellae, and the rate of creation of a fibrillar texture (which is characterized by the dimensionless parameter η) is rather low. An increase in the temperature of thermal treatment, T, enhances melting of transverse lamellae, and, as a consequence, the content of lamellar blocks separated from spherulites monotonically grows. As these blocks are linked with one another only by tie chains, their orientation along the maximal stresses becomes substantially easier, which accelerates the texture formation above the threshold temperature, T^0.

11. Concluding remarks

A series of ten tensile tests with the maximal Hencky strain 0.6 have been performed on iPP at room temperature. Experiments are carried out on injection-molded specimens non-subjected to thermal treatment, as well as annealed for 24 h at several temperature in the range from 110 to 163 °C prior to testing.

Constitutive equations have been derived for the isothermal viscoplastic behavior of a semicrystalline polymer at finite strains. A polymer is treated as an equivalent heterogeneous network of chains bridged by permanent junctions. The network is thought of as an ensemble of MRs linked with each other. In the sub-yield region of deformations, junctions between chains in MRs slide with respect to their reference positions (which reflects sliding of nodes in the amorphous phase and fine slip of lamellar blocks). In the post-yield region of deformations, this sliding process is accompanied by displacements of meso-domains with respect to each other (which reflect coarse slip and fragmentation of lamellar blocks).

Stress–strain relations and kinetic equations for the coarse slip of lamellar blocks are developed by using the laws of thermodynamics. These equations are simplified for uniaxial tension of an incompressible medium. The governing equations are determined by six material constants that are found by fitting the observations. Fair agreement is demonstrated between the experimental stress–strain curves and the results of numerical simulation.

The following conclusions have been drawn:

1. The elastic modulus, C, monotonically grows with the annealing temperature, T, which is explained by an increase in the degree of crystallinity at thermal treatment.
2. The rate of the developed viscoplastic flow (that reflects sliding of junctions in amorphous regions and fine slip of crystalline blocks) weakly increases with T below the critical temperature T_{cr} (which is associated with the second-order phase transition in α spherulites), and strongly grows with T in the post-critical region of temperatures. The strain, ε, that characterizes transition to the steady flow of junctions, decreases with annealing temperature below T_{cr}, and increases afterwards. These observations are explained by a decrease in the degree of lamellar branching with T and by transition to a new mechanism of sliding above the critical temperature.
3. The rate, Γ, of coarse slip and fragmentation of lamellar blocks and the dimensionless parameter, η, that characterizes strain-hardening of a semicrystalline polymer, increase with annealing temperature. Their growth is quite weak below the threshold temperature T^0 (that is associated with disappearance of cross-hatching in α spherulites) and becomes rather strong at $T \geqslant T_{cr}$. These changes are attributed to melting of transverse lamellae that resist formation of oriented micro-fibrils in iPP.

References

Aboulfaraj, M., G'Sell, C., Ulrich, B., Dahoun, A., 1995. In situ observation of the plastic deformation of polypropylene spherulites under uniaxial tension and simple shear in the scanning electron microscope. Polymer 36, 731–742.

Ajji, A., Guevremont, J., Cole, K.C., Dumoulin, M.M., 1996. Orientation and structure of drawn poly(ethylene terephthalate). Polymer 37, 3707–3714.

Alamo, R.G., Brown, G.M., Mandelkern, L., Lehtinen, A., Paukkeri, R., 1999. A morphological study of a highly structurally regular isotactic poly(propylene) fraction. Polymer 40, 3933–3944.

Alberola, N., Fugier, M., Petit, D., Fillon, B., 1995a. Microstructure of quenched and annealed films of isotactic polypropylene. 1. Journal of Materials Science 30, 1187–1195.

Alberola, N., Fugier, M., Petit, D., Fillon, B., 1995b. Tensile mechanical behaviour of quenched and annealed isotactic polypropylene films over a wide range of strain types. 2. Relationship with microstructure. Journal of Materials Science 30, 860–868.

Bergström, J.S., Kurtz, S.M., Rimnac, C.M., Edidin, A.A., 2002. Constitutive modeling of ultra-high molecular weight polyethylene under large-deformation and cyclic conditions. Biomaterials 23, 2329–2343.

Bordonaro, C.M., Krempl, E., 1995. A state variable model for high strength polymers. Polymer Engineering and Science 35, 310–316.

Boyce, M.C., Parks, D.M., Argon, A.S., 1988. Large inelastic deformation of glassy polymers. 1. Rate dependent constitutive model. Mechanics of Materials 7, 15–33.

Boyce, M.C., Socrate, S., Llana, P.G., 2000. Constitutive model for the finite deformation stress–strain behavior of poly(ethylene terephthalate) above the glass transition. Polymer 41, 2183–2201.

Buckley, C.P., Jones, D.P., Jones, D.C., 1996. Hot-drawing of poly(ethylene terephthalate) under biaxial stress, application of a three-dimensional glass–rubber constitutive model. Polymer 37, 2403–2414.

Cho, K., Saheb, D.N., Choi, J., Yang, H., 2002. Real time in situ X-ray diffraction studies on the melting memory effect in the crystallization of β-isotactic polypropylene. Polymer 43, 1407–1416.

Coulon, G., Castelein, G., G'Sell, C., 1998. Scanning force microscopic investigation of plasticity and damage mechanisms in polypropylene spherulites under simple shear. Polymer 40, 95–110.

Drozdov, A.D., Christiansen, J.deC., 2002a. The effect of annealing on the time-dependent behavior of isotactic polypropylene at finite strains. Polymer 43, 4745–4761.

Drozdov, A.D., Christiansen, J.deC., 2002b. The effect of strain rate on the viscoplastic behavior of isotactic polypropylene at finite strains. Preprint cond-mat/0207741.

Drozdov, A.D., Christiansen, J.deC, 2003. The effect of annealing on the elastoplastic response of isotactic polypropylene. European Polymer Journal 39, 21–31.

Eyring, H., 1936. Viscosity, plasticity, and diffusion as examples of absolute reaction rates. Journal of Chemical Physics 4, 283–291.

Gaucher-Miri, V., Seguela, R., 1997. Tensile yield of polyethylene and related copolymers, mechanical and structural evidences of two thermally activated processes. Macromolecules 30, 1158–1167.

Gu, F., Hikosaka, M., Toda, A., Ghosh, S.K., Yamazaki, S., Araki, M., Yamada, K., 2002. Second-order phase transition of high isotactic polypropylene at high temperature. Polymer 43, 1473–1481.

Hasan, O.A., Boyce, M.C., 1995. A constitutive model for the nonlinear viscoelastic viscoplastic behavior of glassy polymers. Polymer Engineering and Science 35, 331–344.

Haupt, P., 2000. Continuum Mechanics and Theory of Materials. Springer, Berlin.

Hiss, R., Hobeika, S., Lynn, C., Strobl, G., 1999. Network stretching, slip processes, and fragmentation of crystallites during uniaxial drawing of polyethylene and related copolymers. A comparative study. Macromolecules 32, 4390–4403.

Iijima, M., Strobl, G., 2000. Isothermal crystallization and melting of isotactic polypropylene analyzed by time- and temperature-dependent small-angle X-ray scattering experiments. Macromolecules 33, 5204–5214.

Inberg, J.P.F., Takens, A., Gaymans, R.J., 2002. Strain rate effects in polycarbonate and polycarbonate/ABS blends. Polymer 43, 2795–2802.

Kalay, G., Bevis, M.J., 1997. Processing and physical property relationships in injection-molded isotactic polypropylene. 2. Morphology and crystallinity. Journal of Polymer Science B: Polymer Physics 35, 265–291.

Kaye, A., Kennett, A.J., 1974. Constrained elastic recovery of a polymeric liquid after various shear flow histories. Rheologica Acta 13, 916–923.

Labour, T., Gauthier, C., Seguela, R., Vigier, G., Bomal, Y., Orange, G., 2001. Influence of the β crystalline phase on the mechanical properties of unfilled and $CaCO_3$-filled polypropylene. 1. Structural and mechanical characterisation. Polymer 42, 7127–7135.

Lima, M.F.S., Vasconcellos, M.A.Z., Samios, D., 2002. Crystallinity changes in plastically deformed isotactic polypropylene evaluated by X-ray diffraction and differential scanning calorimetry methods. Journal of Polymer Science B: Polymer Physics 40, 896–903.

Maiti, P., Hikosaka, M., Yamada, K., Toda, A., Gu, F., 2000. Lamellar thickening in isotactic polypropylene with high tacticity crystallized at high temperature. Macromolecules 33, 9069–9075.

Matthews, R.G., Duckett, R.A., Ward, I.M., Jones, D.P., 1997. The biaxial drawing behaviour of poly(ethylene terephthalate). Polymer 38, 4795–4802.

Meddad, A., Fisa, B., 1997. Stress–strain behavior and tensile dilatometry of glass bead–filled polypropylene and polyamide 6. Journal of Applied Polymer Science 64, 653–665.

Meyer, R.W., Pruitt, L.A., 2001. The effect of cyclic true strain on the morphology, structure, and relaxation behavior of ultra high molecular weight polyethylene. Polymer 42, 5293–5306.

Nitta, K.-H., Takayanagi, M., 1999. Role of tie molecules in the yielding deformation of isotactic polypropylene. Journal of Polymer Science B: Polymer Physics 37, 357–368.

Nitta, K.-H., Takayanagi, M., 2000. Tensile yield of isotactic polypropylene in terms of a lamellar-cluster model. Journal of Polymer Science B: Polymer Physics 38, 1037–1044.

Ran, S., Zong, X., Fang, D., Hsia, B.S., Chu, B., Phillips, R.A., 2001. Structural and morphological studies of isotactic polypropylene fibers during heat/draw deformation by in-situ synchrotron SAXS/WAXD. Macromolecules 34, 2569–2578.

Sabbagh, A.B., Lesser, A.J., 1999. On the phenomena of deformation and neck formation in LLDPE films subjected to uniaxial and biaxial loading conditions. Journal of Polymer Science B: Polymer Physics 37, 2651–2663.

Seguela, R., 2002. Dislocation approach to the plastic deformation of semicrystalline polymers, kinetic aspects for polyethylene and polypropylene. Journal of Polymer Science B: Polymer Physics 40, 593–601.

Seguela, R., Staniek, E., Escaig, B., Fillon, B., 1999. Plastic deformation of polypropylene in relation to crystalline structure. Journal of Applied Polymer Science 71, 1873–1885.

Spathis, G., Kontou, E., 1998. Experimental and theoretical description of the plastic behaviour of semicrystalline polymers. Polymer 39, 135–142.

Staniek, E., Seguela, R., Escaig, B., Francois, P., 1999. Plastic behavior of monoclinic polypropylene under hydrostatic pressure in compressive testing. Journal of Applied Polymer Science 72, 1241–1247.

Suzuki, A., Nakamura, Y., Kunugi, T., 1999. Microstructure and mechanical properties of hot-air drawn poly(ethylene terephthalate) fibers. Journal of Polymer Science B: Polymer Physics 37, 1703–1713.

Sweeney, J., Ward, I.M., 1996. A constitutive law for large deformations of polymers at high temperatures. Journal of the Mechanics and Physics of Solids 44, 1033–1049.

Sweeney, J., Collins, T.L.D., Coates, P.D., Ward, I.M., 1997. Application of an elastic model to the large deformation, high temperature stretching of polypropylene. Polymer 38, 5991–5999.

Sweeney, J., Collins, T.L.D., Coates, P.D., Duckett, R.A., 1999. High-temperature large strain viscoelastic behavior of polypropylene modelled using an inhomogeneously strained network. Journal of Applied Polymer Science 72, 563–575.

Verma, R., Marand, H., Hsiao, B., 1996. Morphological changes during secondary crystallization and subsequent melting in poly(ether ether ketone) as studied by real time small angle X-ray scattering. Macromolecules 29, 7767–7775.

Wagner, M.H., Raible, T., Meissner, J., 1979. Tensile stress overshoot in uniaxial extension of a LDPE melt. Rheologica Acta 18, 427–428.

Wunderlich, B., 1980. Macromolecular Physics. Vol. 3. Crystal Melting. Academic Press, New York.

Yamada, K., Matsumoto, S., Tagashira, K., Hikosaka, M., 1998. Isotacticity dependence of spherulitic morphology of isotactic polypropylene. Polymer 39, 5327–5333.

Zhang, X.C., Butler, M.F., Cameron, R.E., 1999. The relationships between morphology, irradiation and the ductile–brittle transition of isotactic polypropylene. Polymer International 48, 1173–1178.